#### NASA TECHNICAL NOTE



NASA TN D-5334

## CASE FILE COPY

SUPERSONIC AERODYNAMIC CHARACTERISTICS
AND SHOCK STANDOFF DISTANCES FOR
LARGE-ANGLE CONES WITH AND WITHOUT
CYLINDRICAL AFTERBODIES

by James F. Campbell

Langley Research Center

Langley Station, Hampton, Va.

Page Intentionally Left Blank

# SUPERSONIC AERODYNAMIC CHARACTERISTICS AND SHOCK STANDOFF DISTANCES FOR LARGE-ANGLE CONES WITH AND WITHOUT CYLINDRICAL AFTERBODIES

By James F. Campbell

Langley Research Center Langley Station, Hampton, Va.

NATIONAL AERONAUTICS AND SPACE ADMINISTRATION

### Page Intentionally Left Blank

## SUPERSONIC AERODYNAMIC CHARACTERISTICS AND SHOCK STANDOFF DISTANCES FOR LARGE-ANGLE CONES WITH AND WITHOUT CYLINDRICAL AFTERBODIES

By James F. Campbell Langley Research Center

#### SUMMARY

An investigation has been conducted to determine the longitudinal aerodynamic characteristics and shock standoff distances of large-angle cones with and without cylindrical afterbody sections. Cone semiapex angles ranged from  $40^{\circ}$  to  $90^{\circ}$  (disk) and cylindrical afterbody sections ranged in length up to 1.25 times the cone diameter. The tests were performed at Mach numbers from 1.41 to 4.63, at angles of attack from  $-4^{\circ}$  to  $24^{\circ}$ , and at a Reynolds number based on model (base) diameter of  $0.8 \times 10^{6}$ .

Results of this study indicated that all the cone configurations were statically stable with the moment center located at the cone base. Addition of cylindrical afterbody sections resulted in increases in stability throughout the Mach number range. Axial force increased as cone semiapex angle was increased, a maximum being approached for the flat disk. Throughout the angle-of-attack range, addition of cylindrical afterbody sections resulted in reductions in axial force that were not more than 4 percent for all combinations of cone semiapex angles and cylinder lengths and were less than 3 percent for most combinations. Normal force and lift decreased as cone semiapex angle was increased, minimum values being obtained for the flat disk; an increase in these forces resulted when cylindrical afterbody sections were added. Shock standoff distance for any body with a detached shock wave appeared to be uniquely dependent on the inverse square of the density ratio across a normal shock. This dependence allowed shock standoff distance for the conical bodies to be adequately predicted within the test range of cone semiapex angles and Mach numbers.

#### INTRODUCTION

Utilization of unmanned instrumented probes to traverse planetary atmospheres is a natural evolution in our efforts to gather information about the neighboring planets. Studies concerned with entry technology are presented in reference 1 and have provided

information necessary for formulating such a mission. Preliminary designs for an unmanned probe (ref. 2) favor an entry system consisting of an aeroshell device to protect the payload and to provide aerodynamic deceleration during atmospheric entry; the aeroshell is to be separated from the payload at the initiation of the terminal descent system. The uncertainties associated with tenuous atmospheres, such as those of Mars and Venus, suggest a relatively simple aeroshell configuration that minimizes the sensitivity to atmospheric composition. An aeroshell configuration which meets these basic design requirements and which has received much attention recently is the large-angle cone.

Adequate knowledge of the aerodynamic characteristics and shock envelope for the conical aeroshell is a fundamental necessity in the design of the total entry system and provides inputs to studies of flight trajectory and entry dynamics, to estimations of total heat and aerodynamic loads, and to predictions of events associated with aeroshell separation from the payload. The aerodynamic characteristics of conical bodies with semiapex angles up to 60° have been determined in the investigations of references 3 to 5. The study of reference 6 has extended the range of cone semiapex angle up to 90° (flat disk), the results being obtained for Mach numbers from 2.30 to 4.63. Since the large-angle conical aeroshell may be utilized at slower speeds, it is desirable to determine the aerodynamic characteristics and shock standoff distances for cones with semiapex angles up to 90° at lower supersonic Mach numbers than are reported in reference 6.

As shown in previous studies, increasing the semiapex angle of the conical aeroshell increases drag, which provides aerodynamic braking, but decreases the volume capacity for carrying the payload. Since storage and protection of the payload are essential for a successful mission, the use of an afterbody shroud with the conical aeroshell may be necessary. It is appropriate, therefore, to consider the effects of afterbody geometry on the aerodynamic characteristics of large-angle cones.

In an attempt to provide information concerning these problem areas, an investigation has been conducted on a series of cone bodies having semiapex angles ranging from  $40^{\circ}$  to  $90^{\circ}$  (flat disk) at Mach numbers of 1.41 and 2.00. Cylindrical afterbody sections having lengths up to 1.25 times the cone diameter were tested with the same conical bodies at Mach numbers from 1.50 to 4.63. The angle-of-attack range for these tests was  $-4^{\circ}$  to  $24^{\circ}$ , and the Reynolds number based on model (base) diameter was  $0.8 \times 10^{6}$ .

#### SYMBOLS

The results of the tests are presented in coefficient form for both the body and stability axis systems. Data referred to the body axis system pertain to a ballistic type of

entry, whereas data referred to the stability axis system pertain to a lifting type of entry. The pitching-moment reference center is at the cone base on the geometric center line of the cone as shown in figures 1 and 2.

$C_{\mathbf{A}}$	axial-force coefficient, Axial force qS
C <sub>A,b</sub>	base axial-force coefficient, Base axial force qS
$C_{D}$	drag coefficient, $\frac{\text{Drag}}{\text{qS}}$
$C_{\mathrm{L}}$	lift coefficient, $\frac{\text{Lift}}{\text{qS}}$
$c_{L_{lpha}}$	slope of lift curve per degree, $$
$c_{N}$	normal-force coefficient, Normal force
$c_{N\alpha}$	slope of normal-force curve per degree, $\partial C_N/\partial \alpha$

C<sub>m</sub> pitching-moment coefficient, Pitching moment qSD

 $c_{m_{\alpha}}$  slope of pitching-moment curve per degree,  $\partial c_{m}/\partial \alpha$ 

D base diameter of model

k density ratio across normal shock,  $\rho_2/\rho_1$ 

length of cylindrical afterbody section

M free-stream Mach number

q free-stream dynamic pressure

r radius

S base area of model

α angle of attack, degrees

 $\beta$  constant representing rate of change of  $\delta/r_b$  with  $k^{-2}$  (see eq. (1))

- δ standoff distance of detached shock wave, measured along geometric center line of model
- $\epsilon$  constant defined in equation (1)
- $\theta_c$  cone semiapex angle, degrees
- $\xi$  constant defined in equation (1)
- $\rho_1$  density ahead of normal shock
- $\rho_2$  density behind normal shock

#### Subscripts:

att condition for shock attachment

b base

n nose

o conditions at zero angle of attack

s shoulder

#### APPARATUS AND TESTS

#### Models

Details of the cone models are presented in figure 1. The cone models consist of right-circular cones with semiapex angles of 40°, 50°, 60°, 70°, 80°, and 90° (flat disk); they were constructed of polished aluminum and had pointed noses and flat bases. Diameter for all the models was 4.80 inches (12.19 centimeters). These models, with the exception of the 50° cone, were utilized in the cone investigation of reference 6. The cylindrical afterbody sections mated to the cone models (fig. 2) were also constructed of polished aluminum. Each of the cylindrical sections had a flat base and a diameter to match that of the cone. Typical model installation of the cone and cone-cylinder configurations is shown in the photographs of figure 3. Sting length was four times the model base diameter to minimize the sting length effects noted in reference 6.

#### Tunnels

Tests were conducted in the three test sections associated with the Langley 4- by 4- foot supersonic pressure tunnel and the Langley Unitary Plan wind tunnel. Both of these wind tunnels are continuous-flow systems having variable-pressure capability. The nozzle leading to the test section of the 4- by 4-foot tunnel is symmetrical and may be manually changed to provide Mach numbers from about 1.4 to 2.2. The Unitary Plan wind tunnel has two test sections, both of which are 4 feet (1.22 meters) square and approximately 7 feet (2.13 meters) long. The nozzles leading to these test sections are of the asymmetric sliding-block type which permits a continuous variation in Mach number from 1.5 to 2.9 in the low Mach number test section and from 2.3 to 4.7 in the high Mach number test section.

#### Test Conditions and Measurements

The cone models without cylindrical afterbody sections were tested at Mach numbers of 1.41 and 2.00 and with cylindrical afterbody sections at Mach numbers of 1.50, 2.00, 2.30, 2.50, and 4.63. The angle-of-attack range for these tests was from about  $-4^{\circ}$  to  $24^{\circ}$  at zero sideslip, and the Reynolds number based on model (base) diameter was  $0.8 \times 10^{6}$ . The cone-cylinder configurations tested during the course of this investigation are shown schematically in figure 4. Each configuration is identified by one or more letters which correspond to the test conditions summarized in the following table:

Test condition	Mach number	Total pressure		Dynamic pressure		Stagnation temperature	
		lb/ft <sup>2</sup>	kN/m <sup>2</sup>	lb/ft <sup>2</sup>	$kN/m^2$	$\circ_{\mathbf{F}}$	oK
a	1.41	993.0	47.545	428.0	20.493	110.0	316.5
	2.00	1200.0	57.456	429.0	20.541	110.0	316.5
b	1.50	1112.0	53.243	477.0	22.839	150.0	338.7
	2.00	1325.0	63.441	473.0	22.647	150.0	338.7
	2.50	1689.0	80.869	433.0	20.732	150.0	338.7
c	2.30	1532.0	73.353	453.0	21.690	150.0	338.7
	4.63	5275.0	252.568	232.0	11.108	175.0	352.6

Stagnation dewpoint was maintained below  $-30^{\circ}$  F (239° K) to avoid significant condensation effects in the test sections.

Aerodynamic forces and moments were measured by means of an electrical straingage balance housed partially in the cone models. The aft end of the balance which extended behind the base of the models was enclosed in a sleeve so that it was protected from any flow gradients. For the largest-angle cones ( $\theta_{\rm C}=70^{\rm o}$ ,  $80^{\rm o}$ , and  $90^{\rm o}$ ) which had little or no model volume in which to attach the balance, a permanent extension was affixed to the model base (fig. 1); this extension served as the attachment point and protective sleeve for the balance. It is believed that this extension had no significant effect on the data presented in this paper.

The axial-force values presented herein represent the gross measurements made by the strain-gage balance and are not corrected for base pressure.

Angles of attack have been corrected for both tunnel-flow angularity and deflection of the balance and sting due to aerodynamic loads.

Boundary-layer trips were not affixed to the models.

#### RESULTS AND DISCUSSION

#### Cone

Aerodynamic characteristics. - The variation of longitudinal aerodynamic characteristics with angle of attack is presented in figures 5 and 6 for the family of conical bodies. These data indicate that all the configurations are statically stable  $(-C_{m_{\alpha}})$ , pitchingmoment coefficient being nearly linear throughout the angle-of-attack range. Cones having semiapex angles equal to or greater than 60° have pitching-moment-curve slopes and magnitudes that are little different throughout the angle-of-attack range. This is illustrated in the summary plots of figure 7 where pitching-moment-curve slope at  $\alpha = 0^{\circ}$ is shown as a function of cone semiapex angle for the two test Mach numbers. As noted, an increase in Mach number results in a slight decrease in stability for all the cones. This trend becomes more meaningful when complemented by the higher Mach number results (M > 2.0) of reference 6, as shown in figure 8(a). These data indicate that a decrease in stability occurs with increase in Mach number for Mach numbers less than that for shock attachment, and an increase in stability with increase in Mach number for Mach numbers greater than that for shock attachment.  $(M_{att} = 1.95 \text{ and } 3.11 \text{ for }$  $\theta_{\rm c}$  = 40° and 50°, respectively.) The curve representing the 60° cone is typical of the stability trends for cones having larger semiapex angles for which the shock wave is detached at all Mach numbers.

The variation of normal-force coefficient with angle of attack for the cone configurations (figs. 5 and 6) is seen to be essentially linear. As cone semiapex angle is increased, there is a corresponding decrease in normal-force coefficient such that for the flat disk ( $\theta_c = 90^\circ$ ) normal-force coefficient goes to zero. Similar trends of normal-force-curve slope at zero angle of attack  $C_{N_{\alpha,0}}$  with cone semiapex angle are seen in figure 7. Increasing Mach number from 1.41 to 2.00 results in increases in  $C_{N_{\alpha,0}}$  for the  $40^\circ$  cone, normal-force-curve slope being essentially unchanged for the other cone

configurations. This trend of normal-force-curve slope with Mach number is shown in figure 8(b) in conjunction with the higher Mach number data of reference 6 (M > 2.0). The increase of  $C_{N_{\alpha,0}}$  with Mach number for the  $40^{\circ}$  and  $50^{\circ}$  cones occurs at, or near, the Mach number corresponding to shock attachment. The respective values of  $C_{N_{\alpha,0}}$  for cones with semiapex angles equal to or greater than  $60^{\circ}$  are unchanged in the range of Mach numbers.

The basic data of figures 5 and 6 indicate that maximum axial-force coefficient (and drag) generally occurs at angles of attack near zero for the conical bodies. An increase in axial-force coefficient at intermediate angles of attack (compared with that at zero angle of attack) is noted for the cones with the largest semiapex angles. This increase in axial-force coefficient is accredited to the increase in base drag experienced by the cones at intermediate angles of attack, as demonstrated in figure 9 for an 80° cone configuration. Increasing cone semiapex angle (figs. 5 and 6) results in increases in axial-force coefficient throughout the angle-of-attack range, a maximum being obtained for the flat disk  $(\theta_c = 90^\circ)$  configuration. This trend is illustrated in the summary plots of figure 7 where axial-force coefficient at zero angle of attack is shown as a function of cone semiapex angle. Increasing Mach number from 1.41 to 2.00 causes an increase in CA, o throughout the range of cone semiapex angles, except the 40° cone which showed little effect. This trend of axial-force coefficient with Mach number is shown in figure 8(a) in conjunction with the higher Mach number trends presented in reference 6. These data imply that an increase in Mach number for Mach numbers greater than that for shock attachment results in a decrease in CA, o.

As seen from the basic data of figures 5 and 6, lift-curve slope is negative for all the conical configurations. Increasing cone semiapex angle results in decreases in lift-curve slope, a maximum negative value being obtained for the flat disk. (See fig. 7.) The effects of Mach number on lift-curve slope can be seen in figure 8(b) and are reflections of the aforementioned effects of Mach number on normal-force-curve slope and axial force.

Shock standoff distance. Schlieren photographs of the cone models at zero angle of attack are presented in figure 10. Shock standoff distance obtained from these photographs is plotted in figure 11 as a function of cone semiapex angle. These data show that an increase in cone semiapex angle results in a regular increase in  $\delta/r_b$ , whereas an increase in Mach number from 1.41 to 2.00 results in decreases in  $\delta/r_b$ . Similar trends of shock standoff distance with cone semiapex angle and Mach number were noted in the investigation of reference 6 for Mach numbers from 2.30 to 4.63.

In an attempt to empirically describe shock standoff distance as a function of Mach number, the experimental data of this investigation, of reference 3, and of references 6 to 9 are plotted in figure 12 against the inverse square of the density ratio across a

normal shock  $(\rho_2/\rho_1)^{-2} = k^{-2}$ . Plotting the data in this fashion results in a linear variation of  $\delta/r_b$  with  $k^{-2}$  for all the cones; therefore, the shock standoff distance for each cone appears to be uniquely dependent on  $k^{-2}$ . Expressing shock standoff distance in the equation for a straight line gives

$$\frac{\delta}{r_b} = \beta (k^{-2} - \epsilon) + \xi \tag{1}$$

where  $\beta$  represents the rate of change of  $\delta/r_b$  with  $k^{-2}$ , and  $\xi$  represents the shock standoff distance at a given value of  $k^{-2}$  (=  $\epsilon$ ).

The constants in equation (1) were evaluated at M = 4.63 for each of the cones except for the  $40^{\circ}$  and  $50^{\circ}$  cones; the constants for these two cones were evaluated at the respective shock attachment Mach numbers, M = 1.95 and 3.11.

These constants are listed as follows:

$\theta_{\rm c}$ , deg	β	€	ξ
40	1.60	0.1488	0
50	2.15	.0640	0
60	2.65	.0423	.05
70	2.95	.0423	.21
80	3.04	.0423	.39
90	3.04	.0423	.55

Using these constants in equation (1) yields estimates of shock standoff distance which are in good agreement with the experimental data presented in figure 12. In order to obtain shock standoff distance as a function of Mach number, normal-shock relations for a perfect gas are used in equation (1) to obtain

$$\frac{\delta}{r_b} = \beta \left( \frac{1}{36} + \frac{5}{18} \text{ M}^{-2} + \frac{25}{36} \text{ M}^{-4} - \epsilon \right) + \xi \tag{2}$$

Curves generated by this expression are presented in figure 13 along with the experimental data and are seen to adequately predict the magnitudes and trends of shock standoff distance with Mach number for all cone models.

In order to empirically describe shock standoff distance as a function of Mach number and cone semiapex angle, it is necessary to replace those constants in equation (2) which are functions of cone semiapex angle ( $\beta$  and  $\xi$ ) by expressions describing their relation with  $\theta_{\rm C}$  ( $\beta = \beta(\theta_{\rm C})$  and  $\xi = \xi(\theta_{\rm C})$ ). The values of  $\beta$  used in equation (2) are plotted in figure 14 against cone semiapex angle; the resulting variation of  $\beta$  with  $\theta_{\rm C}$  suggests a second-order polynomial equation of the following type:

$$\beta = A \sin^2 \theta_C + B \sin \theta_C + C \tag{3}$$

The conditions used to evaluate the constants in this equation are:

At 
$$\theta_{\rm C} = 90^{\rm O}$$
,  $\beta = 3.04$   
At  $\theta_{\rm C} = 60^{\rm O}$ ,  $\beta = 2.65$   
At  $\theta_{\rm C} = 40^{\rm O}$ ,  $\beta = 1.60$ 

Imposing these conditions on equation (3) yields

$$\beta = -5.029 \sin^2 \theta_{\rm C} + 12.292 \sin \theta_{\rm C} - 4.224 \tag{4}$$

The curve generated by this expression is seen in figure 14 to provide a good estimation of the variation of  $\beta$  with  $\theta_c$ .

To obtain an expression relating the constant  $\xi$  (eq. (2)) to cone semiapex angle, it should be recalled that  $\xi$  is simply the shock standoff distance for a particular cone semiapex angle at a given Mach number. Since equation (2) has shown the capability of predicting the magnitude of shock standoff distance for all the cone semiapex angles of this investigation, this expression was used to calculate values of  $\delta/r_b$  associated with the conical bodies at M=2.00. Plotting these values of  $\delta/r_b$  as a function of  $\theta_c$  (fig. 15) leads to the assumption of a linear variation of  $\delta/r_b$  with  $\theta_c$ , and the following equation is obtained:

$$\xi = \frac{\delta}{r_b} = 1.5485 \frac{\theta_c}{900} - 0.69856 \tag{5}$$

where

$$\epsilon = k^{-2} = 0.141$$

The values of  $\delta/r_b$  obtained from equation (5) are in good agreement with those values obtained from equation (2). (See fig. 15.) It should be mentioned that equation (5) satisfies the condition that at M=2.00 shock attachment occurs on a cone having a semiapex angle of  $40.6^{\circ}$ .

Expressions have now been obtained describing the constants  $\beta$  and  $\xi$  in equation (2) as functions of cone semiapex angle. Substituting equations (4) and (5) into equation (2) with  $\epsilon = 0.141$  gives the following empirical expression describing shock stand-off distance as a function of Mach number and cone semiapex angle

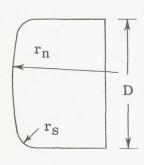
$$\frac{\delta}{r_{b}} = \left(-5.029 \sin^{2}\theta_{c} + 12.292 \sin\theta_{c} - 4.224\right) \left(\frac{5}{18} M^{-2} + \frac{25}{36} M^{-4} - 0.11322\right) + 1.5485 \frac{\theta_{c}}{90^{\circ}} - 0.69856$$
(6)

Values of shock standoff distance generated by this equation are plotted in figure 13 and show only slight deviations from those values predicted by equation (2). From equation (6), shock standoff distance for a particular cone semiapex angle becomes essentially a linear function of  $1/M^2$  as Mach number becomes large; this condition agrees with the results of reference 6 for  $M \ge 2.30$ . For  $M \to \infty$ , equation (6) reduces to

$$\frac{\delta}{r_b} = 0.5694 \sin^2 \theta_c - 1.3917 \sin \theta_c + 1.5485 \frac{\theta_c}{900} - 0.2203$$

Shock standoff distance for the  $60^{\circ}$  to  $90^{\circ}$  cones at  $M=\infty$  are shown in figure 13 estimated by this expression and the method of reference 10.

The results of the preceding analysis raise the question as to whether shock standoff distance for any body with a detached shock wave is uniquely dependent on the inverse



square of the density ratio across a normal shock. An indication of the answer to this question is provided by the data of references 11 and 12 which resulted from tests on a series of blunt bodies having various nose and shoulder radii. (See the sketch.) A plot of shock standoff distance against  $k^{-2}$  for the family of blunt bodies having an infinite nose radius and finite values of shoulder radius (fig. 16) shows linear trends similar to those previously noted for the conical bodies (fig. 12). These results

substantiate the premise that shock standoff distance is a function of the inverse square of the density ratio across a normal shock for all blunt bodies.

An empirical expression describing shock standoff distance as a function of Mach number and shoulder radius can be obtained in the same manner as was done previously for Mach number and cone semiapex angle. The resulting equation is

$$\frac{\delta}{r_b} = \beta \left( \frac{5}{18} \text{ M}^{-2} + \frac{25}{36} \text{ M}^{-4} - 0.01452 \right) - 0.780 \frac{r_s}{D} + 0.550$$
 (7)

and  $\beta$ , the rate of change of  $\delta/r_b$  with  $k^{-2}$ , is presented in figure 17 as a function of shoulder radius. The linear nature of shock standoff distance with shoulder radius at M=4.63 is used in equation (2) to yield equation (7). This empirical approach predicts values of shock standoff distance  $\delta/r_b$  that are in good agreement with the experimental results for the range of Mach number and shoulder radius considered. (See fig. 18.) It

should be noted that the  $\delta/r_b$  values predicted by equation (7) for the flat disk  $(r_s/D=0)$  are the same as those values predicted by equation (6) for  $\theta_c = 90^{\circ}$ .

#### Aerodynamic Characteristics of Cone Cylinder

Schlieren photographs are presented in figures 19 and 20 for selected cone-cylinder models at several angles of attack. The longitudinal aerodynamic characteristics of the cone-cylinder configurations tested during the course of this investigation are presented in figures 21 to 37; data for conical models with semiapex angles from 60° to 90° (ref. 6) are presented at M = 2.30 and 4.63 for comparison. These data indicate that the cones with no cylindrical afterbody (l/D = 0) are statically stable  $(-C_{mo})$  at all test Mach numbers; addition of cylindrical afterbody sections to the cone bodies results in a progressive increase in stability. This trend of stability with cylinder length is demonstrated in figure 38 where pitching-moment-curve slope at zero angle of attack is shown as a function of cylinder length for all test Mach numbers. The 40° cone configuration has the minimum level of stability throughout the range of cylinder lengths. The stability of the largest angle cone-cylinder configurations is affected by a separated flow region at the shoulder of the cone-cylinder body. (See schlieren photographs of figs. 19 and 20.) The result of this separated flow region is evidenced as a decreasing effectiveness of the cylinder to produce pitching moment  $(C_{m_{\alpha,0}})$  at l/D = 0.50 minus  $C_{m_{\alpha,0}}$  at l/D = 0with increasing cone semiapex angle, particularly at the lower test Mach numbers. These trends are substantiated by the schlieren photographs which show the intensification of the separated flow region with increase in semiapex angle and decrease in Mach number. The effectiveness of the cylindrical afterbody to produce increases in stability is seen in the summary plots of figure 39 to decrease with increase in Mach number.

Addition of cylindrical afterbody sections to the conical bodies (figs. 21 to 35) produces increases in normal-force coefficient throughout the angle-of-attack range. This is reflected in increases in normal-force-curve slope at zero angle of attack as seen in the summary plots of figure 40. The  $40^{\circ}$  cone-cylinder configuration has the largest values of normal-force-curve slope throughout the range of cylinder lengths. Increasing cone semiapex angle for the configurations with l/D=0.50 has effects on  $C_{N\alpha,0}$  similar to those for the cone bodies with no cylinder length (l/D=0) as discussed previously. At M=2.00 and 2.30, the effect of cone semiapex angle on  $C_{N\alpha,0}$  is greatly reduced for cylinder lengths greater than l/D=0.50; at M=4.63, the effect of  $\theta_{\rm C}$  on  $C_{N\alpha,0}$  is generally independent of cylinder length. The aforementioned separated flow region is noted to have an effect on the normal-force-producing capability of the cylinder, particularly at M=2.00 and 2.30; this is evidenced as a decreasing effectiveness of the cylinder to produce normal force  $(C_{N\alpha,0}$  at l/D=0.50 minus  $C_{N\alpha,0}$  at l/D=0 with increasing cone semiapex angle. This trend diminishes with Mach number increase resulting in a constant increase in  $C_{N\alpha,0}$  with increase in l/D at M=4.63 for all

the cone semiapex angles. The effect of Mach number on  $C_{N_{\alpha,0}}$  is presented in figure 41 and shows that the increase in  $C_{N_{\alpha,0}}$  associated with increase in cylinder length is reduced with increase in Mach number for most of the cone semiapex angles.

Addition of cylindrical afterbody sections results in only small reductions in axial-force coefficient throughout the angle-of-attack range. (See figs. 21 to 35.) These reductions are not more than 4 percent for all combinations of cone semiapex angles and cylinder lengths and are less than 3 percent for most combinations. Effects on drag coefficient of increasing the cylinder length are similar to those noted on axial-force coefficient for angles of attack near zero. At the highest angles of attack, increasing cylinder length leads to increases in drag coefficient; this increase is a result of the large increases in normal-force coefficient associated with increased cylinder length. The effects on cone semiapex angle and cylinder length on axial-force coefficient (and drag) at zero angle of attack are shown in the summary plots of figure 42. Since the cone-cylinder configurations have  $C_{A,0}$  values that are little different from those of the cones with no cylinder, the trends of  $C_{A,0}$  with Mach number are similar to the trends in figure 8(a) for the cones.

The basic data of figures 21 to 35 show that addition of cylindrical afterbody sections results in increases in lift coefficient throughout the angle-of-attack range. The resulting increase in lift-curve slope at zero angle of attack with increase in cylinder length is shown in figure 43. The effects on  $CL_{\alpha,0}$  of increasing cone semiapex angle and/or cylinder length are similar to those previously discussed for  $CN_{\alpha,0}$ . The effect of Mach number on lift-curve slope is presented in figure 44 and shows that the effectiveness of the cylindrical afterbody sections to produce lift is greatest at the lowest test Mach number.

#### CONCLUSIONS

A study has been conducted to determine the supersonic longitudinal aerodynamic characteristics and shock standoff distances of a series of conical bodies with and without cylindrical afterbody sections. Cone semiapex angles ranged from 40° to 90° (disk) and the cylindrical afterbody sections ranged in length up to 1.25 times the cone diameter. Results of this study led to the following conclusions:

- 1. All the cone configurations were statically stable with the moment center located at the cone base. Addition of cylindrical afterbody sections resulted in increases in stability throughout the Mach number range.
- 2. Axial force increased as cone semiapex angle was increased, a maximum being obtained for the flat disk. Throughout the angle-of-attack range, addition of cylindrical afterbody sections results in reductions in axial force that were not more than 4 percent

for all combinations of cone semiapex angles and cylinder lengths and were less than 3 percent for most combinations.

- 3. Normal force and lift decreased as cone semiapex angle was increased, minimum values being obtained for the flat disk; an increase in these forces resulted with the addition of cylindrical afterbody sections.
- 4. Shock standoff distance for any body with a detached shock wave appeared to be uniquely dependent on the inverse square of the density ratio across a normal shock. This dependence allowed shock standoff distance for the conical bodies to be adequately predicted within the test range of cone semiapex angles and Mach numbers.

Langley Research Center,

National Aeronautics and Space Administration, Langley Station, Hampton, Va., April 21, 1969, 124-07-03-12-23.

#### REFERENCES

- 1. Eggers, Alfred J., Jr., ed.: Atmosphere Entry. Volume I of AIAA Selected Reprint Series, [1967].
- 2. Roberts, Leonard: Entry Into Planetary Atmospheres. Astronaut. Aeronaut., vol. 2, no. 10, Oct. 1964, pp. 22-29.
- 3. Campbell, James F.: Longitudinal Aerodynamic Characteristics of Several High-Drag Bodies at Mach Numbers From 1.50 to 4.63. NASA TN D-3915, 1967.
- 4. Nichols, James O.; and Nierengarten, Edward A.: Aerodynamic Characteristics of Blunt Bodies. Tech. Rep. No. 32-677 (Contract NAS 7-100), Jet Propulsion Lab., California Inst. Technol., Nov. 19, 1964.
- 5. Owens, Robert V.: Aerodynamic Characteristics of Spherically Blunted Cones at Mach Numbers From 0.5 to 5.0. NASA TN D-3088, 1965.
- 6. Campbell, James F.; and Howell, Dorothy T.: Supersonic Aerodynamics of Large-Angle Cones. NASA TN D-4719, 1968.
- 7. Johnston, G. W.: An Investigation of the Flow About Cones and Wedges at and Beyond the Critical Angle. Rep. No. 24, Inst. Aerophys., Univ. of Toronto, Dec. 1952.
- 8. Boison, J. Christopher; and Curtiss, Howard A.: An Experimental Investigation of Blunt Body Stagnation Point Velocity Gradient. ARS J., vol. 29, no. 2, Feb. 1959, pp. 130-135.
- 9. Serbin, H.: Hypersonic, Non-Viscous Flow Around a Circular Disk Normal to the Stream. U.S. Air Force Proj. RAND Res. Mem. RM-1713, RAND Corp., May 3, 1956.
- 10. Aleksenko, I. I.; Barantsev, R. G.; and Panteleyeva, I. N.: The Method of Transverse Approximation in a Hypersonic Flow. FTD-TT-65-1806, U.S. Air Force, Jan. 6, 1966. (Available from DDC as AD 626968.)
- 11. Stallings, Robert L., Jr.: Experimentally Determined Local Flow Properties and Drag Coefficients for a Family of Blunt Bodies at Mach Numbers From 2.49 to 4.63. NASA TR R-274, 1967.
- 12. Lees, Lester: Recent Developments in Hypersonic Flow. Jet Propulsion, vol. 27, no. 11, Nov. 1957, pp. 1162-1178.

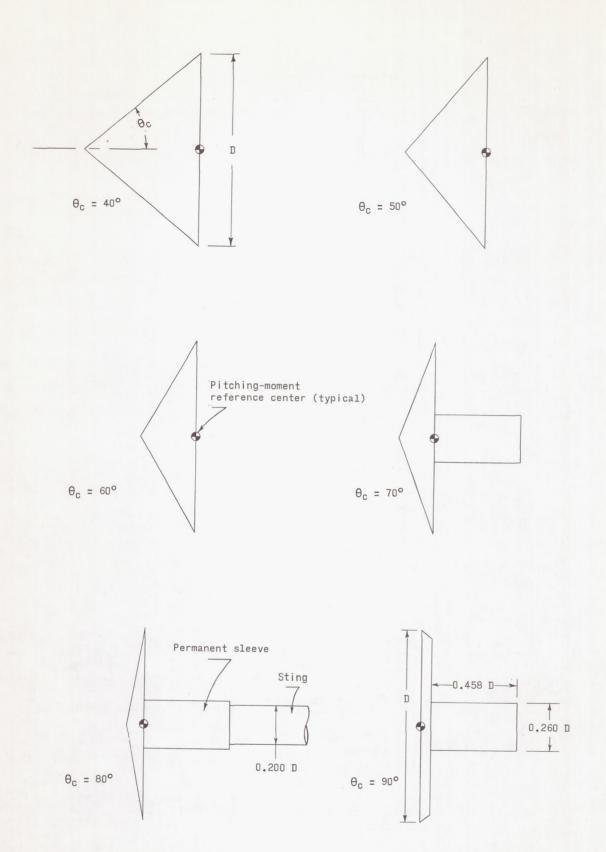


Figure 1.- Details of cone models. Dimensions are presented as fractions of base diameter D which is 4.80 in. (12.19 cm).

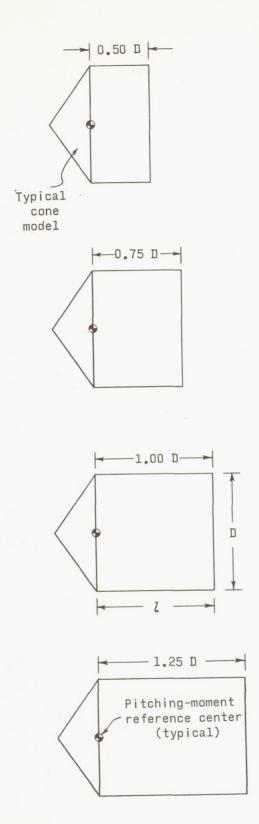
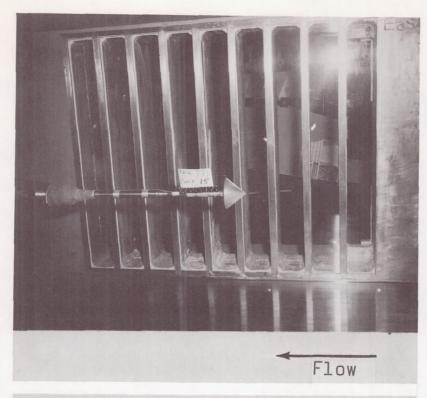


Figure 2.- Details of cylindrical afterbody sections. Dimensions are presented as fractions of base diameter D which is 4.80 in. (12.19 cm).



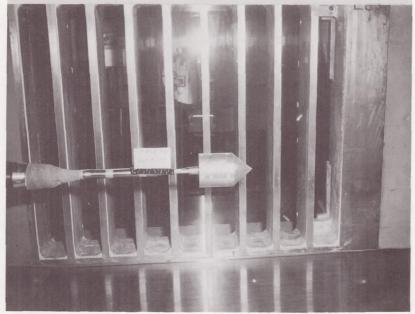


Figure 3.- Typical cone and cone-cylinder models installed in the test section.

L-69-1362

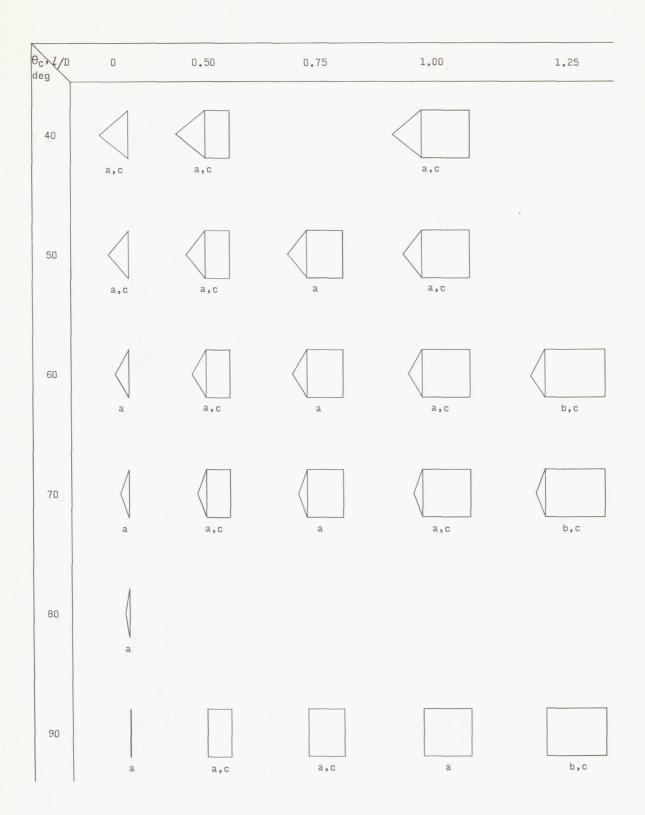


Figure 4.- Test configurations. Letters correspond to test conditions in table on page 5.

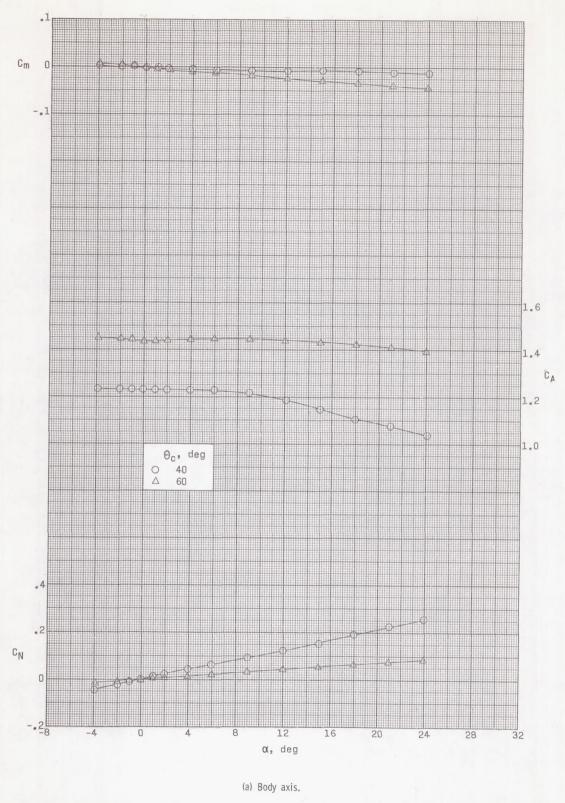
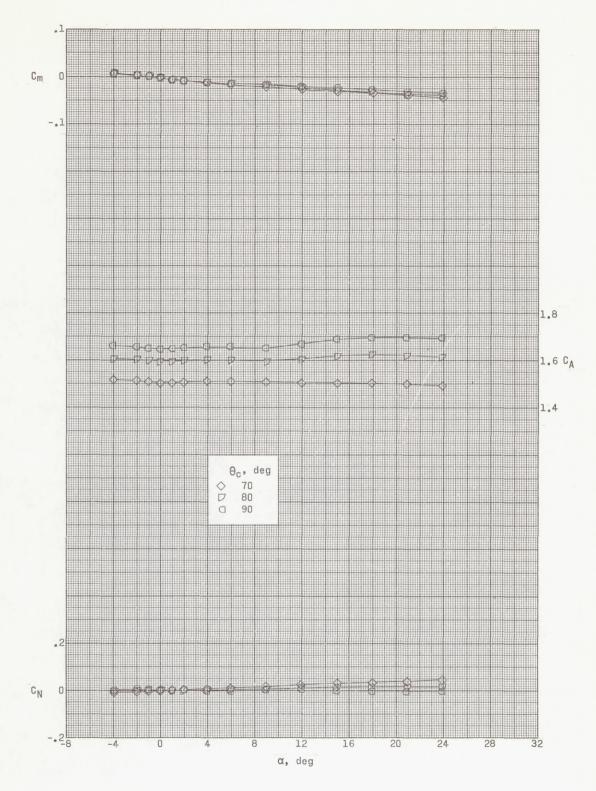
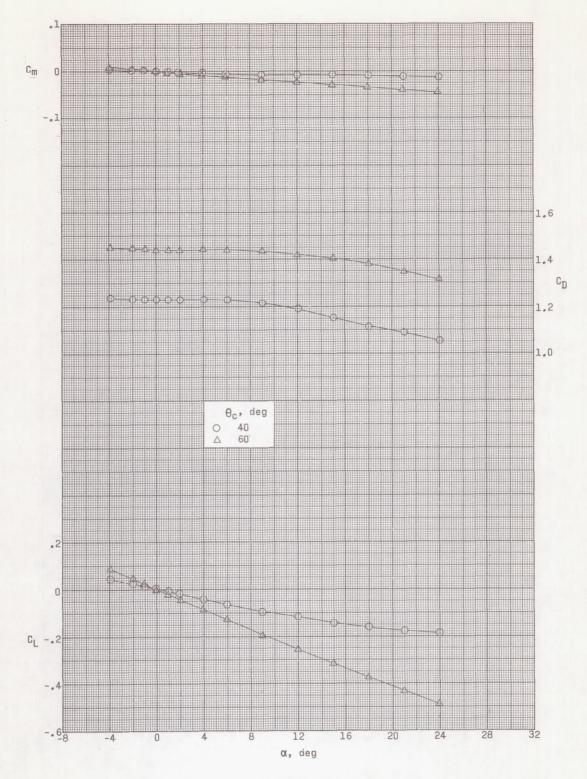


Figure 5.- Variation of longitudinal characteristics with angle of attack for family of cone models. I/D = 0; M = 1.41.



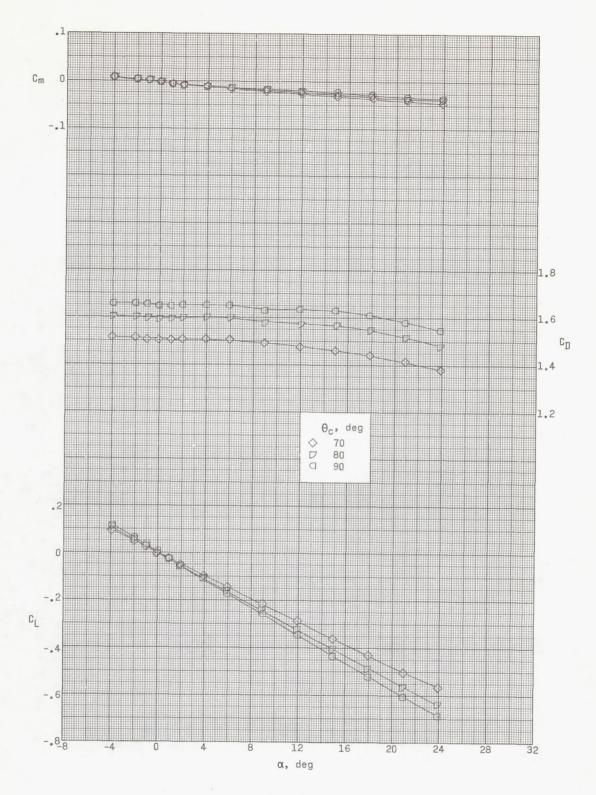
(a) Concluded.

Figure 5.- Continued.



(b) Stability axis.

Figure 5.- Continued.



(b) Concluded.

Figure 5.- Concluded.

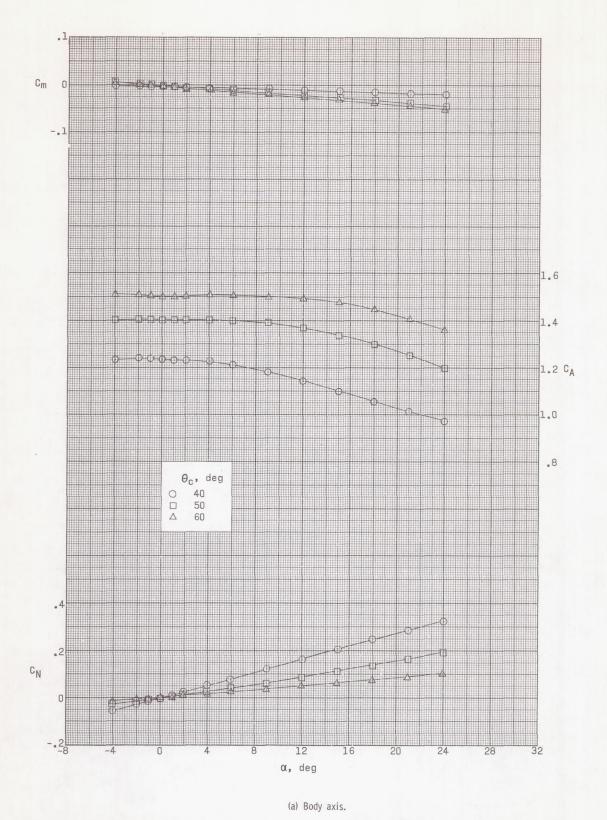
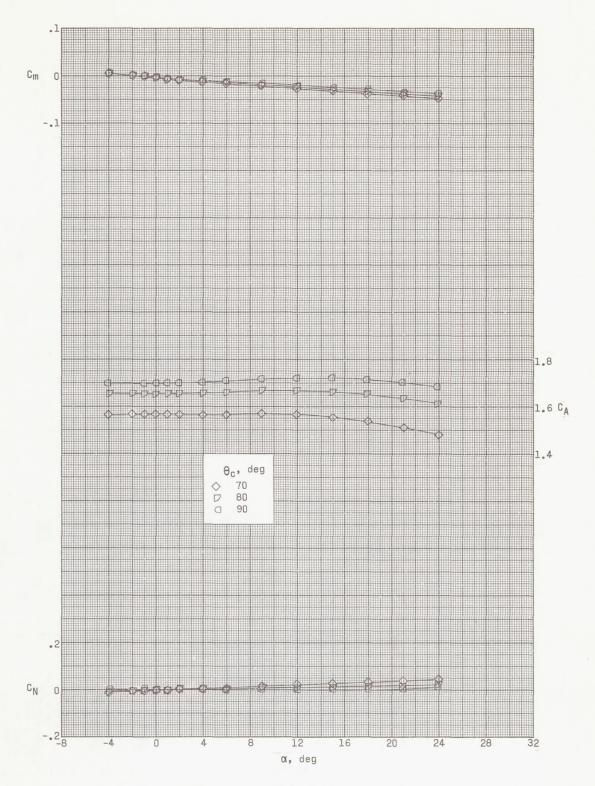
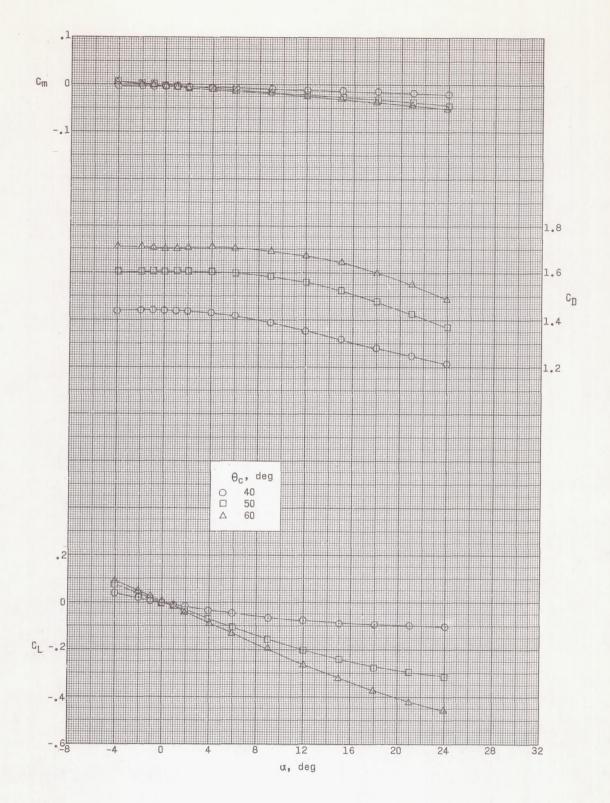


Figure 6.- Variation of longitudinal characteristics with angle of attack for family of cone models. I/D = 0; M = 2.00.

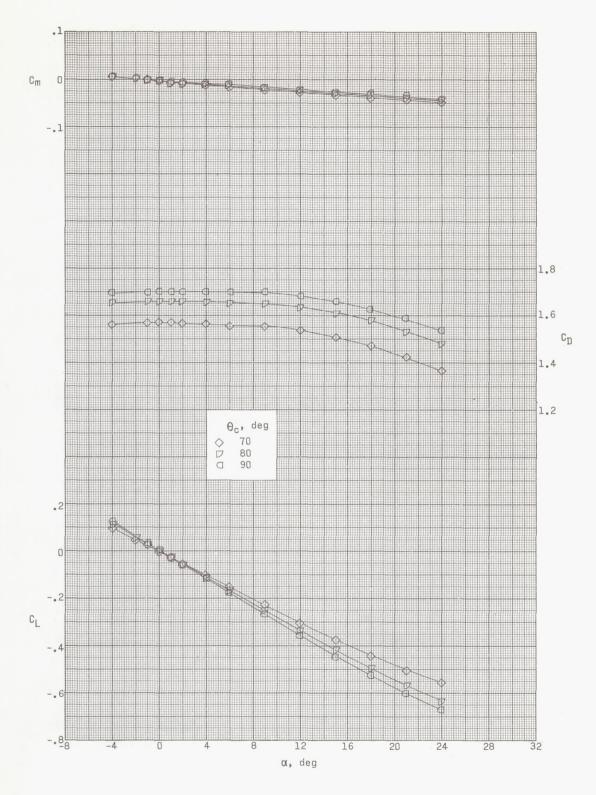


(a) Concluded. Figure 6. - Continued.



(b) Stability axis.

Figure 6.- Continued.



(b) Concluded.

Figure 6.- Concluded.

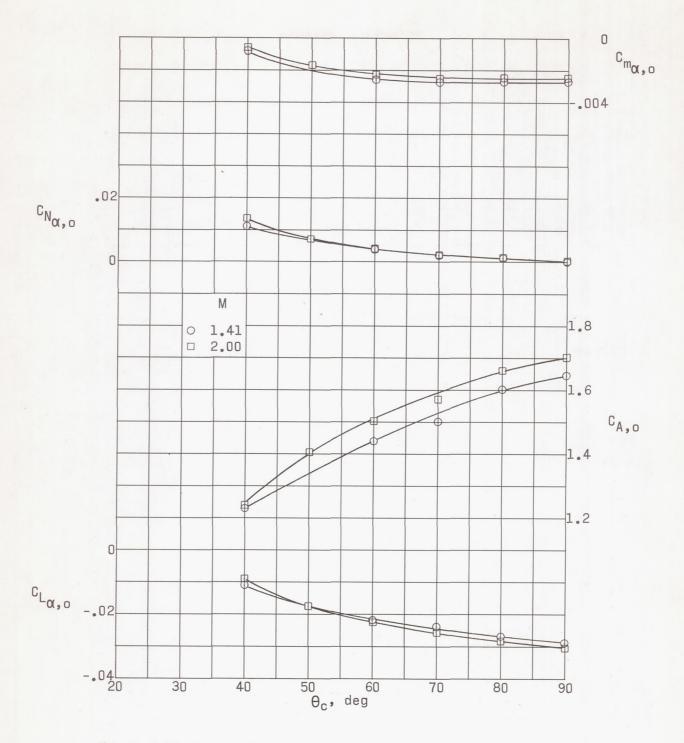


Figure 7.- Variation of aerodynamic parameters at zero angle of attack with cone semiapex angle. I/D = 0.

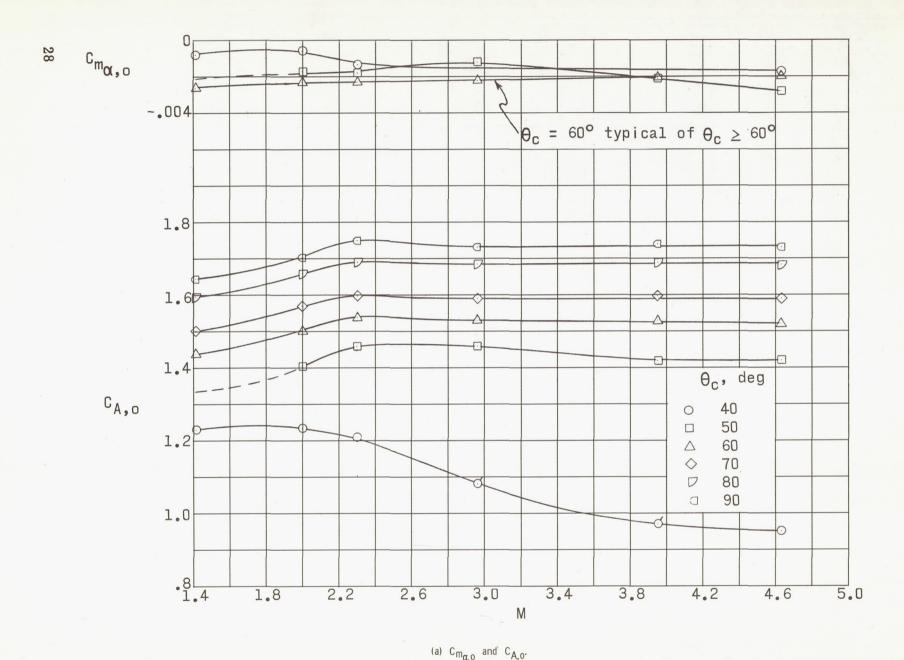
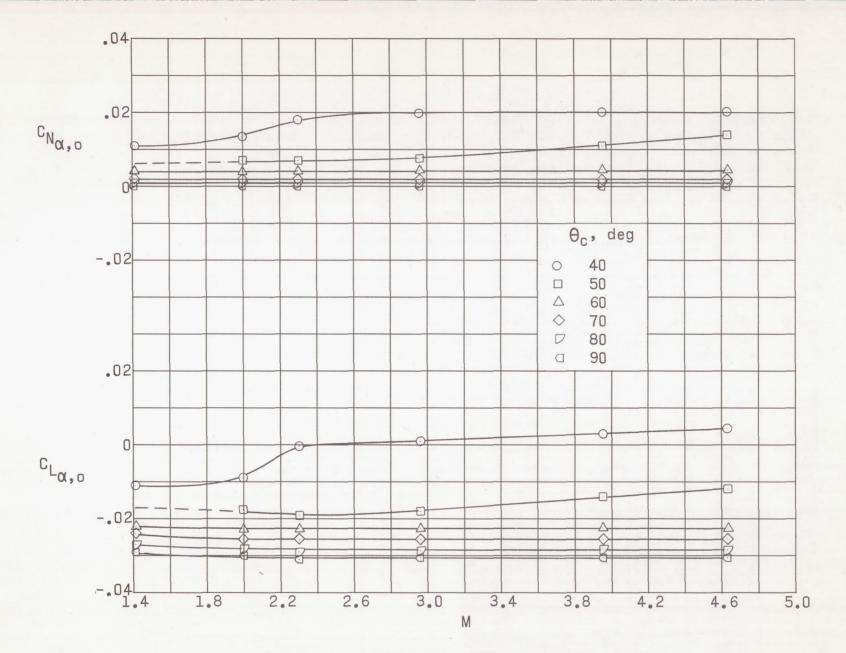


Figure 8.- Variation of aerodynamic parameters at zero angle of attack with Mach number. 1/D = 0; data for M > 2.0 from reference 6; ticked symbols from reference 4.



(b)  $C_{N_{\alpha,0}}$  and  $C_{L_{\alpha,0}}$ . Figure 8.- Concluded.

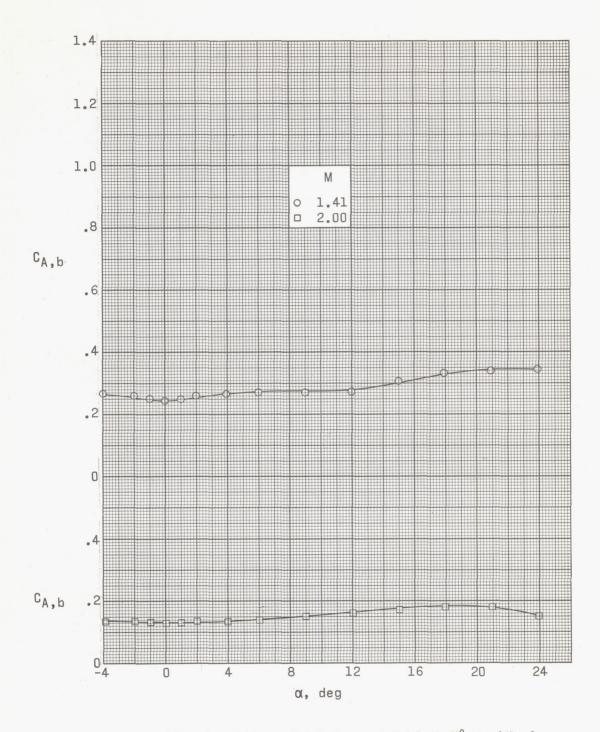
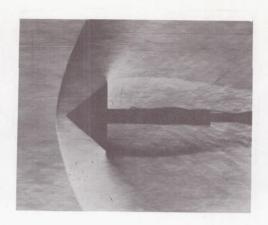


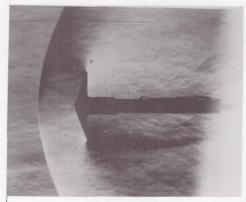
Figure 9.- Variation of base axial-force coefficient with angle of attack for the  $80^{\circ}$  cone. l/D = 0.



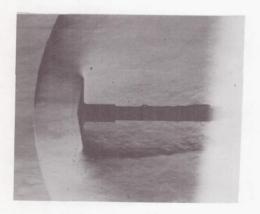
 $\theta_{\rm C}$  = 40°



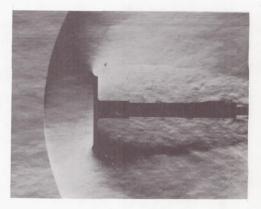
 $\theta_{\rm c}$  = 60°



 $\theta_c = 70^{\circ}$ 



θ<sub>c</sub> = 80°

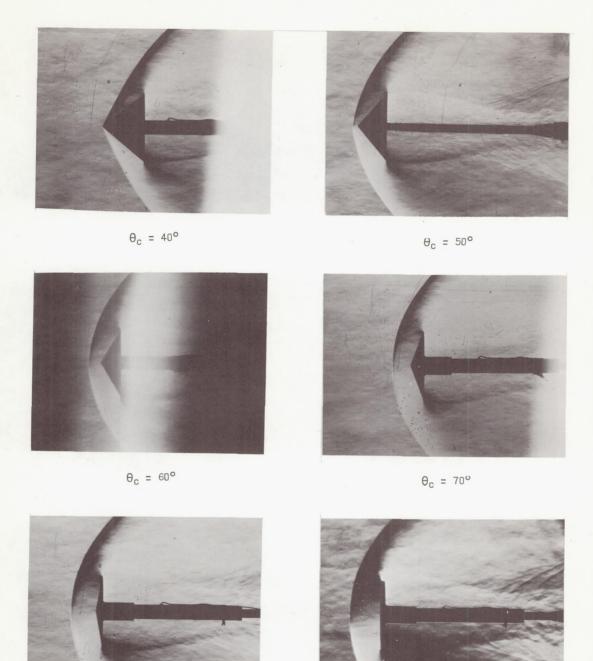


 $\theta_c = 90^{\circ}$ 

(a) M = 1.41.

L-69-1363

Figure 10.- Schlieren photographs of cone models at zero angle of attack.



(b) M = 2.00. Figure 10.- Concluded.

 $\theta_{\rm c}$  = 80°

L-69-1364

θ<sub>c</sub> = 90°

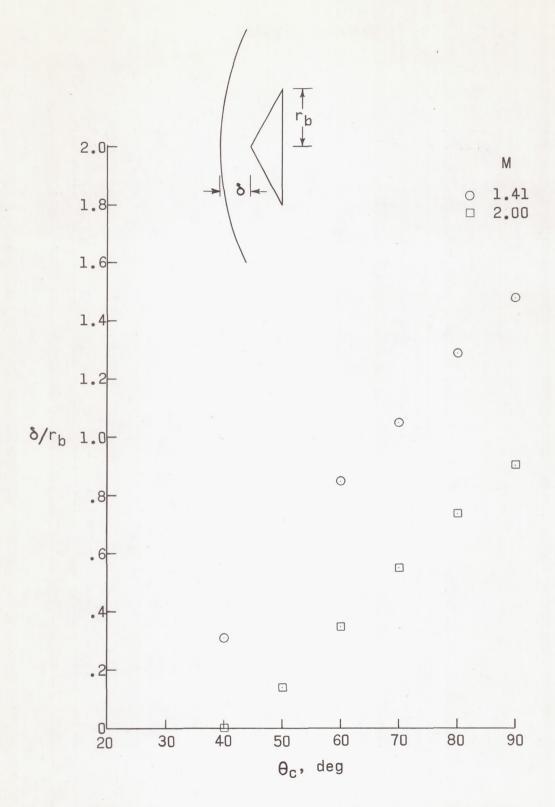


Figure 11.- Variation of nondimensionalized shock standoff distance with cone semiapex angle.

## Experiment

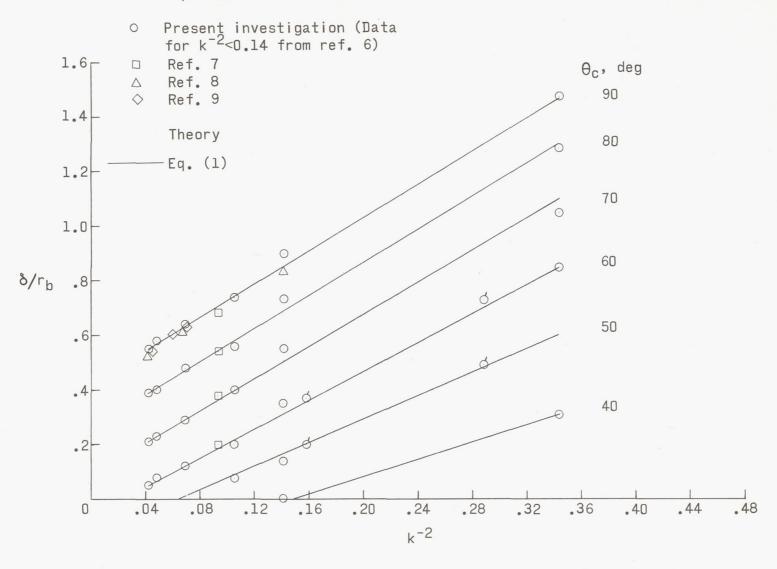


Figure 12.- Variation of nondimensionalized shock standoff distance with inverse square of density ratio across normal shock for family of conical bodies. Ticked symbols from reference 3.

## Experiment O Present investigation (Data for M>2.0 from ref. 6) Ref. 7 Ref. 8 Ref. 9 Theory Eq. (2) ---Eq. (6) Ref. 10

- D

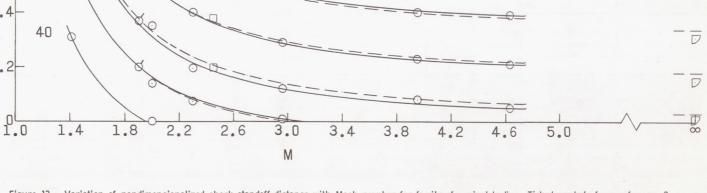


Figure 13.- Variation of nondimensionalized shock standoff distance with Mach number for family of conical bodies. Ticked symbols from reference 3.

 $1.6\overline{\Theta}_{c}$ , deg

1.4

1.2

1.0

δ/r<sub>b</sub> .8

90

80

70

60

50

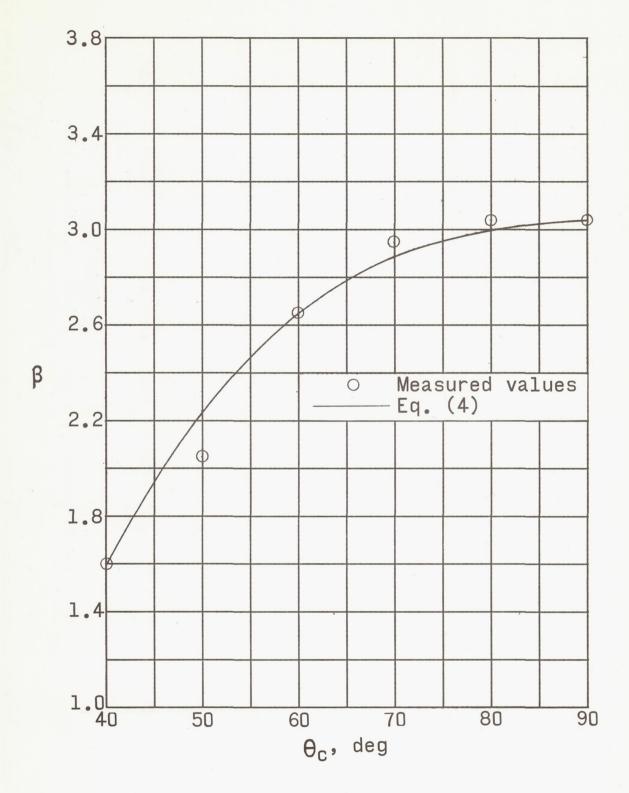


Figure 14.- Correlation of  $\beta$ , rate of change of  $\delta/r_b$  with  $k^{-2}$ , as function of cone semiapex angle.

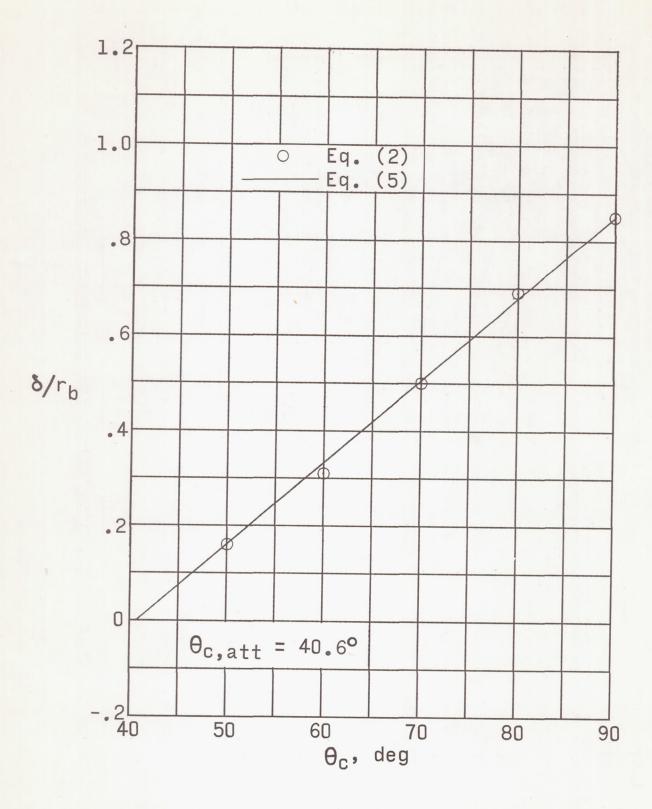


Figure 15.- Correlation of nondimensionalized shock standoff distance as a function of cone semiapex angle. M = 2.00.

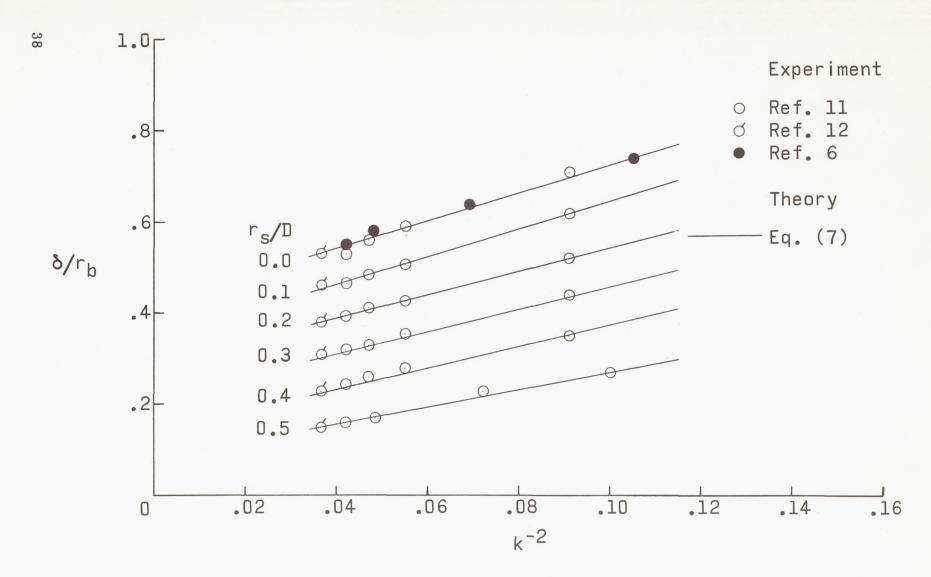


Figure 16.- Variation of nondimensionalized shock standoff distance with inverse square of density ratio across normal shock for family of blunt bodies having various shoulder radii.  $r_n/D = \infty$ .

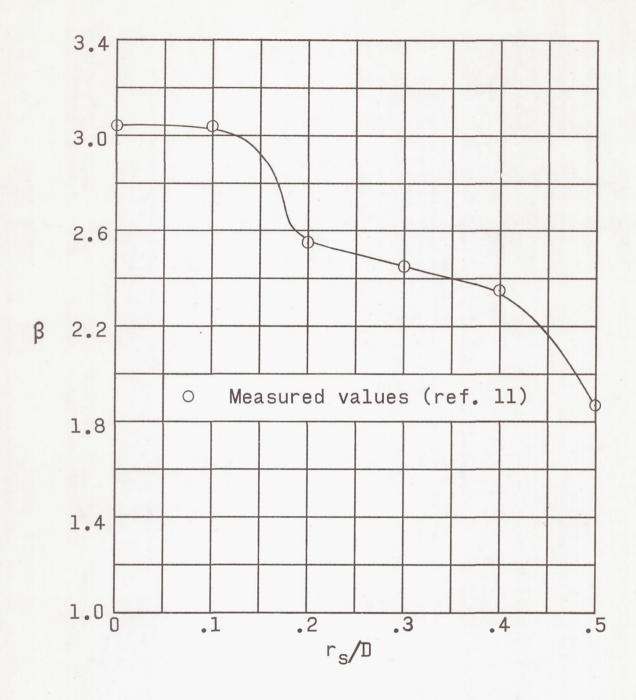


Figure 17.- Effect of shoulder radius on  $\,\beta,$  the rate of change of  $\,\delta/r_b\,$  with  $\,k^{-2}.$ 

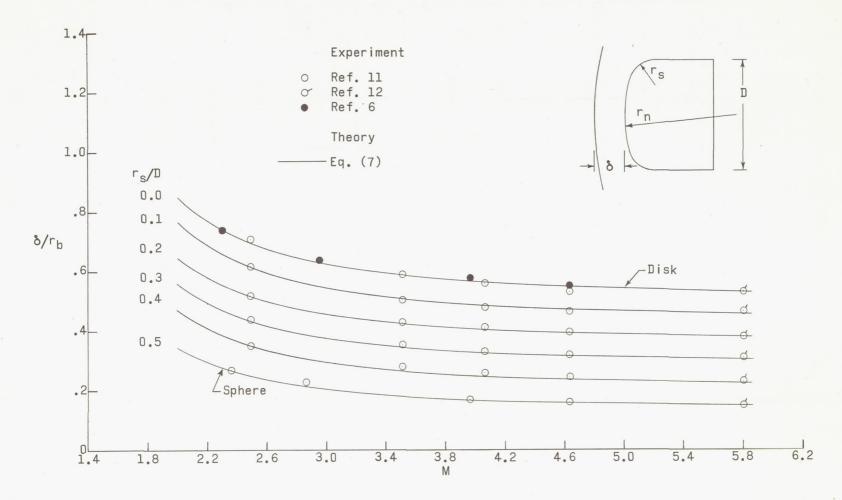


Figure 18.- Variation of nondimensionalized shock standoff distance with Mach number for family of blunt bodies having various shoulder radii.  $r_n/D = \infty$ 

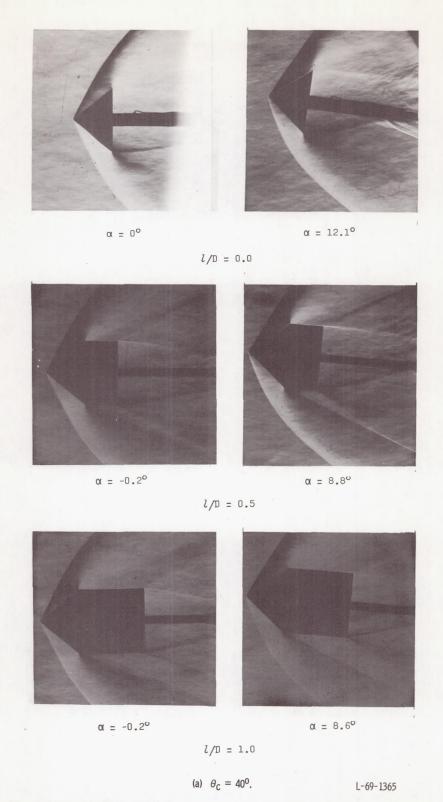


Figure 19.- Schlieren photographs of selected cone-cylinder models at several angles of attack and M = 2.00.



 $\alpha = 0^{\circ}$ 



 $\alpha = -0.2^{\circ}$ 



α = 8.8°

l/D = 0.5



 $\alpha = -0.2^{\overline{0}}$ 

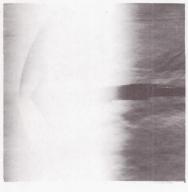


 $\alpha = 8.7^{\circ}$ 

l/D = 1.0

(b)  $\theta_{\rm C} = 50^{\rm O}$ .

Figure 19.- Continued.

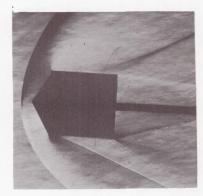


 $\alpha = 0^{\circ}$ 

 $\alpha = 12.0^{\circ}$ 

l/D = 0.0





 $\alpha = -0.2^{\circ}$ 

α = 8.7°

l/D = 1.0

(c) 
$$\theta_{\rm C} = 60^{\rm O}$$
.

L-69-1367

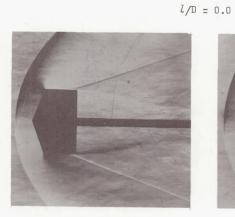
Figure 19.- Continued.



 $\alpha = 0^{\circ}$ 



 $\alpha = 12.0^{\circ}$ 



 $\alpha = -0.2^{\circ}$ 



 $\alpha = 8.8^{\circ}$ 



 $\alpha = -0.2^{\circ}$ 



 $\alpha = 8.7^{\circ}$ 

(d)  $\theta_{\rm C} = 70^{\rm O}$ .

l/D = 1.0

l/D = 0.5

Figure 19.- Continued.



α = 0°



 $\alpha = 12.0^{\circ}$ 



 $\alpha = -0.2^{\circ}$ 



 $\alpha = 8.8^{\circ}$ 

l/D = 0.5



 $\alpha = -0.2^{\circ}$ 



 $\alpha = 8.7^{\circ}$ 

l/D = 1.0

(e)  $\theta_{\rm C} = 90^{\circ}$ .

Figure 19.- Concluded.

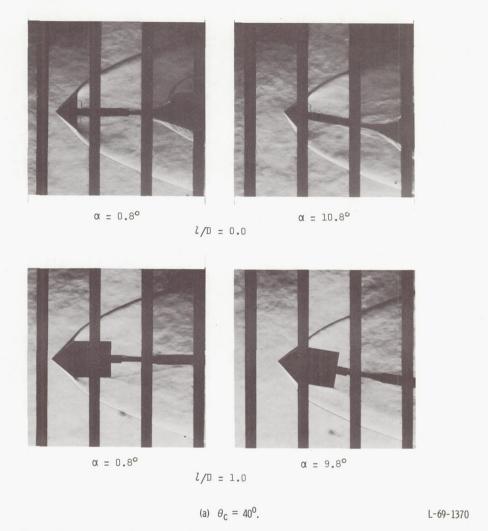


Figure 20.- Schlieren photographs of selected cone-cylinder models at several angles of attack and  $\,M=4.63.\,$ 



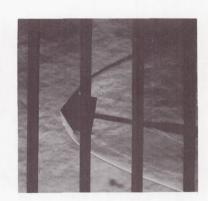
 $\alpha = 0.9^{\circ}$ 



 $\alpha = 9.9^{\circ}$ 

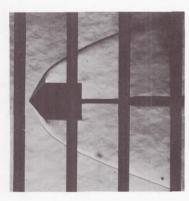


 $\alpha = 0.8^{\circ}$ 



 $\alpha = 9.9^{\circ}$ 

l/D = 0.5



 $\alpha = 0.7^{\circ}$ 



 $\alpha = 9.8^{\circ}$ 

l/D = 1.0

(b)  $\theta_{\rm C} = 50^{\rm O}$ .

Figure 20.- Continued.



 $\alpha = 0.8^{\circ}$ 



 $\alpha = 9.5^{\circ}$ 



 $\alpha = 0.9^{\circ}$ 



 $\alpha = 9.9^{\circ}$ 

l/D = 0.5



 $\alpha = 0.8^{\circ}$ 



 $\alpha = 9.8^{\circ}$ 

l/D = 1.0

(c)  $\theta_{\rm C} = 60^{\rm O}$ .

Figure 20.- Continued.



 $\alpha = -1.0^{\circ}$ 



α = 9.1°



 $\alpha = 1.3^{\circ}$ 



 $\alpha = 10.3^{\circ}$ 

(d)  $\theta_{\rm C} = 70^{\rm O}$ . Figure 20.- Continued.



 $\alpha = 0^{\circ}$ 

l/D = 0.0

 $\alpha = 9.0^{\circ}$ 





 $\alpha = 0.4^{\circ}$ 

l/D = 0.5

 $\alpha = 9.4^{\circ}$ 

(e)  $\theta_{\rm C} = 90^{\rm O}$ .

Figure 20.- Concluded.

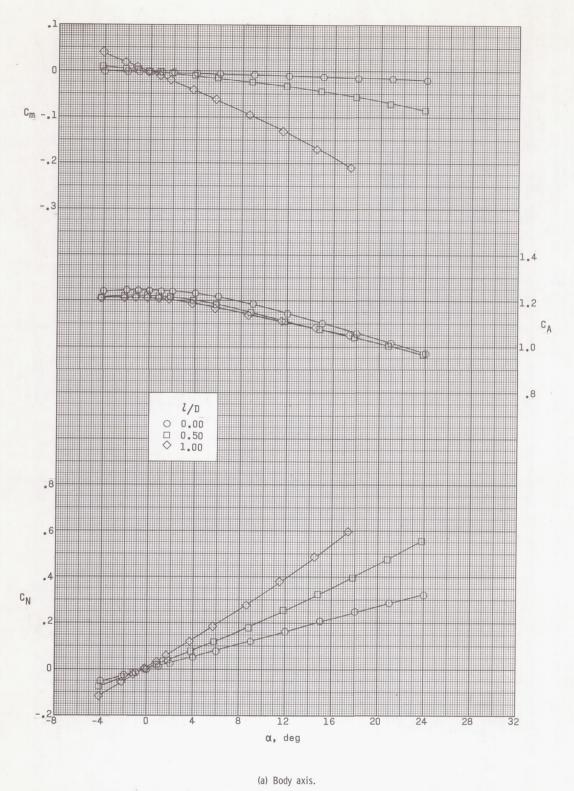
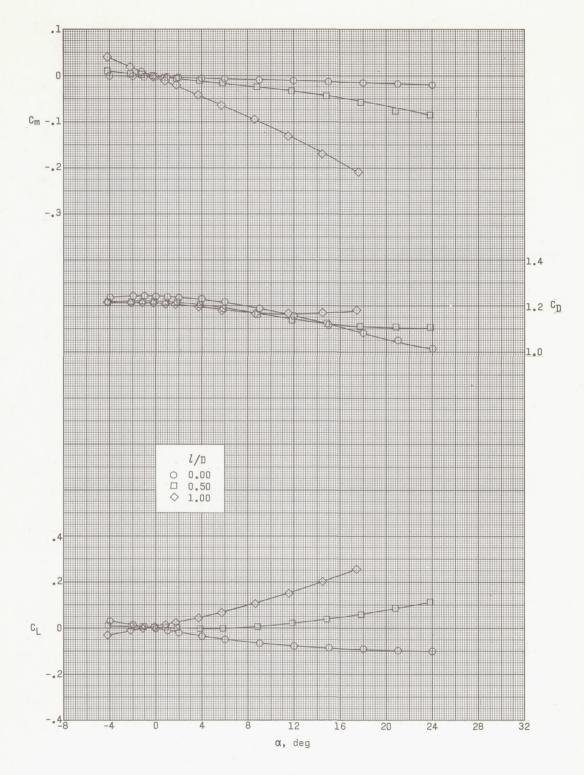


Figure 21.- Effect of cylinder length on longitudinal aerodynamic characteristics of  $40^{\circ}$  semiapex angle cone at M = 2.00.



(b) Stability axis.

Figure 21.- Concluded.

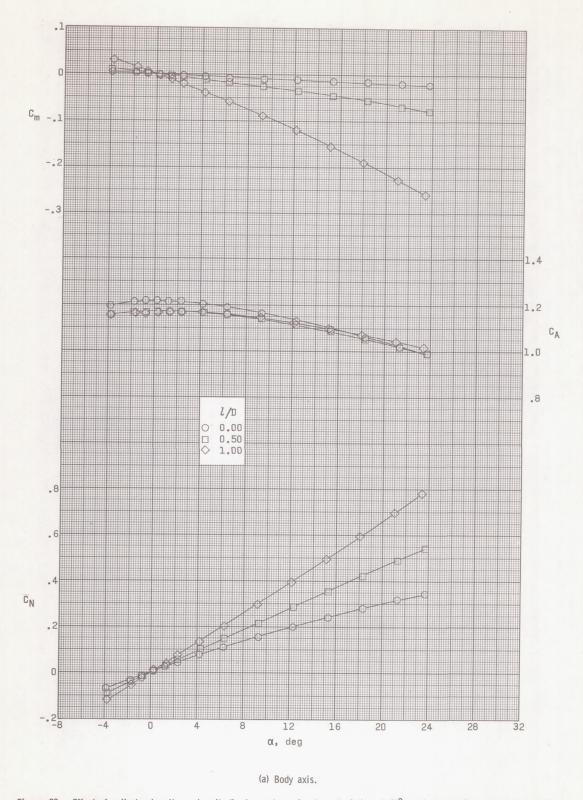
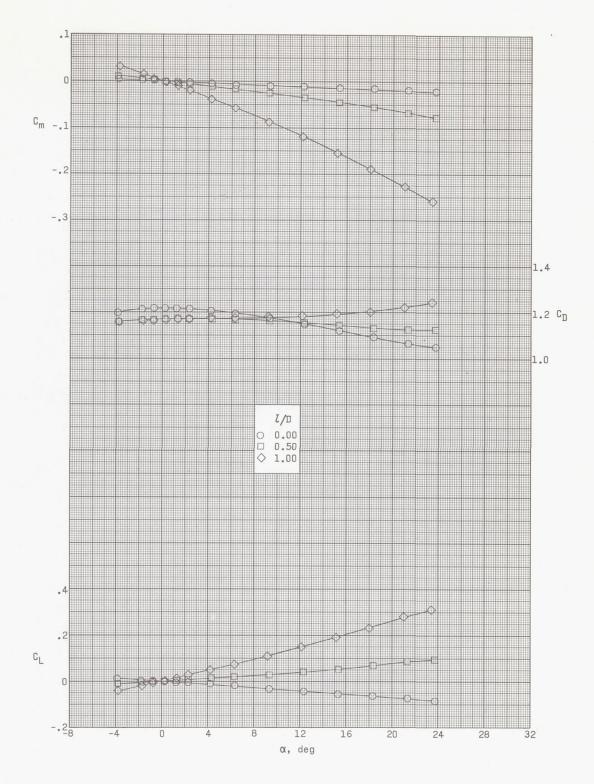


Figure 22.- Effect of cylinder length on longitudinal aerodynamic characteristics of  $40^{\circ}$  semiapex angle cone at M = 2.30.



(b) Stability axis.

Figure 22.- Concluded.

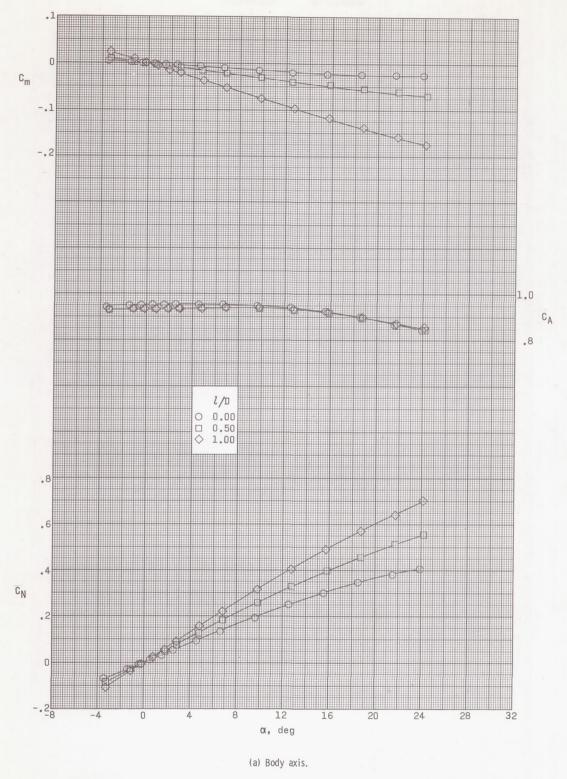
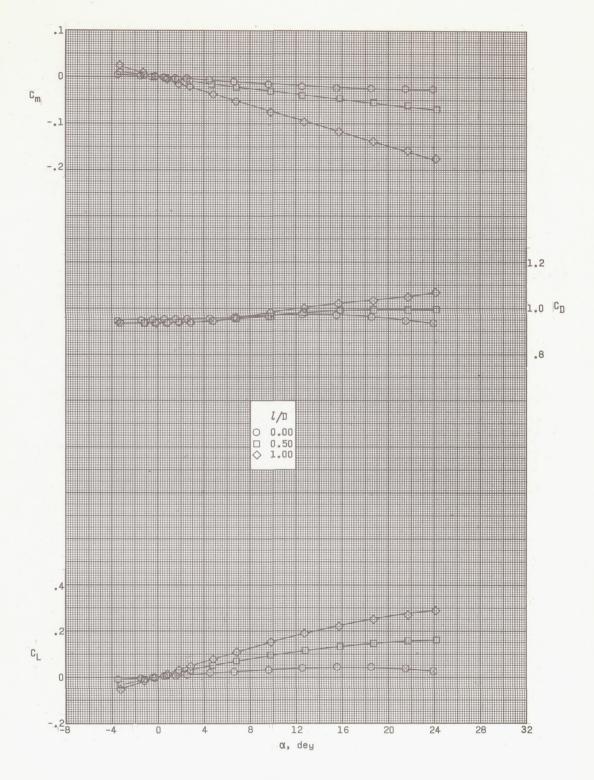


Figure 23.- Effect of cylinder length on longitudinal aerodynamic characteristics of  $40^{\circ}$  semiapex angle cone at M = 4.63.



(b) Stability axis.

Figure 23.- Concluded.

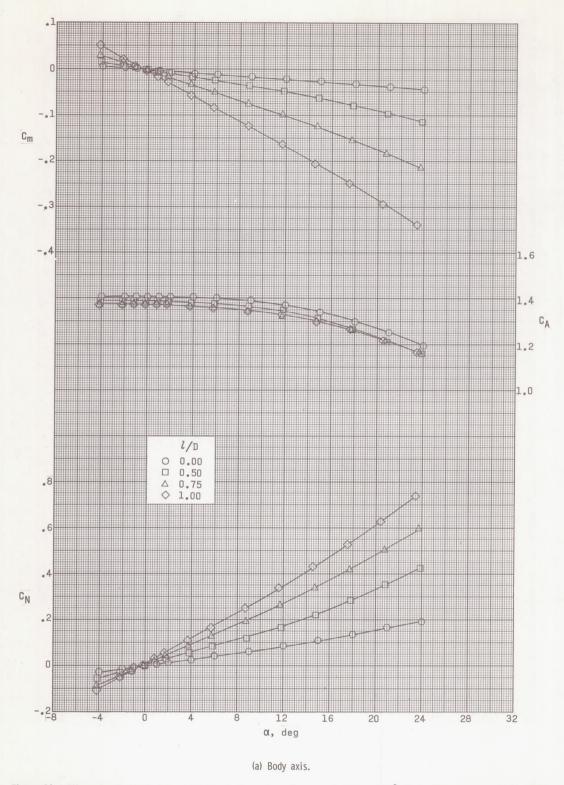
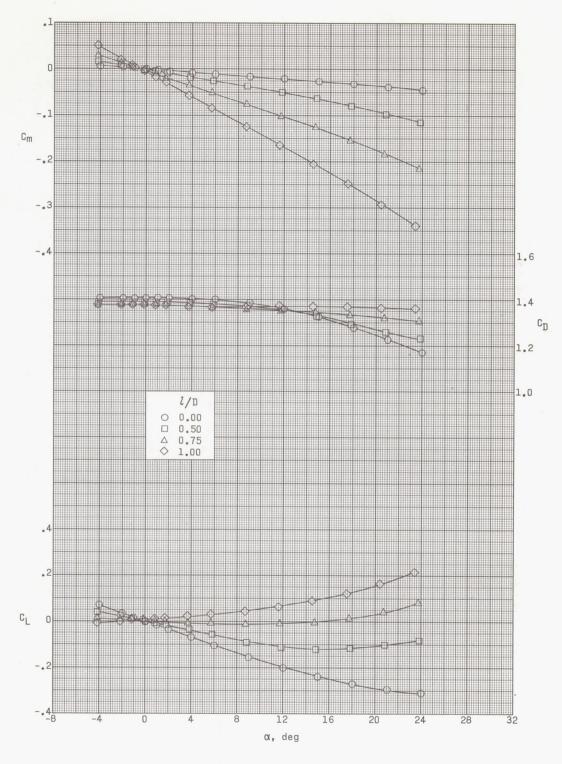


Figure 24.- Effect of cylinder length on longitudinal aerodynamic characteristics of  $50^{\circ}$  semiapex angle cone at M = 2.00.



(b) Stability axis.

Figure 24.- Concluded.

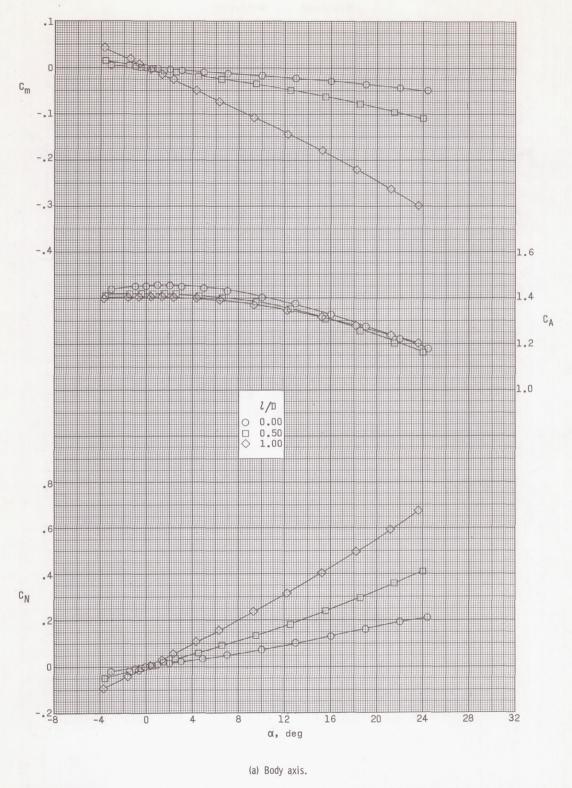
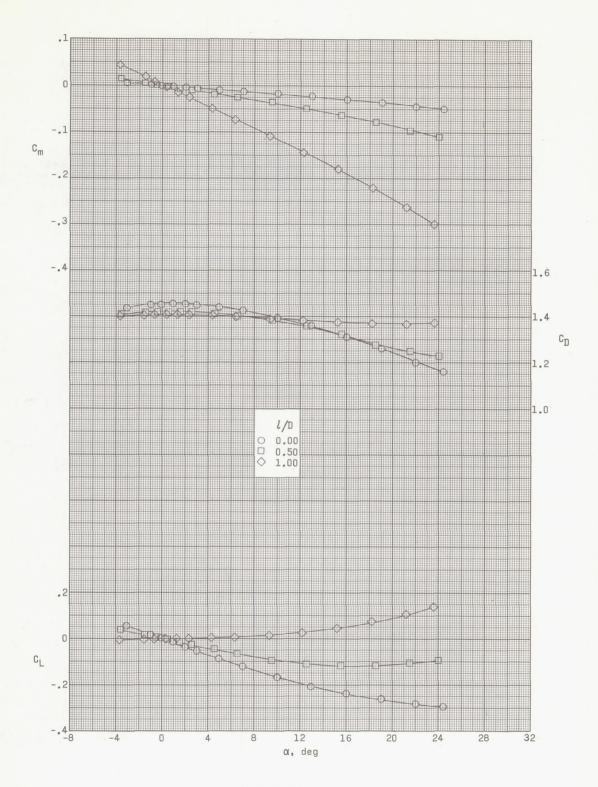


Figure 25.- Effect of cylinder length on longitudinal aerodynamic characteristics of  $50^{\circ}$  semiapex angle cone at M = 2.30.



(b) Stability axis.

Figure 25.- Concluded.

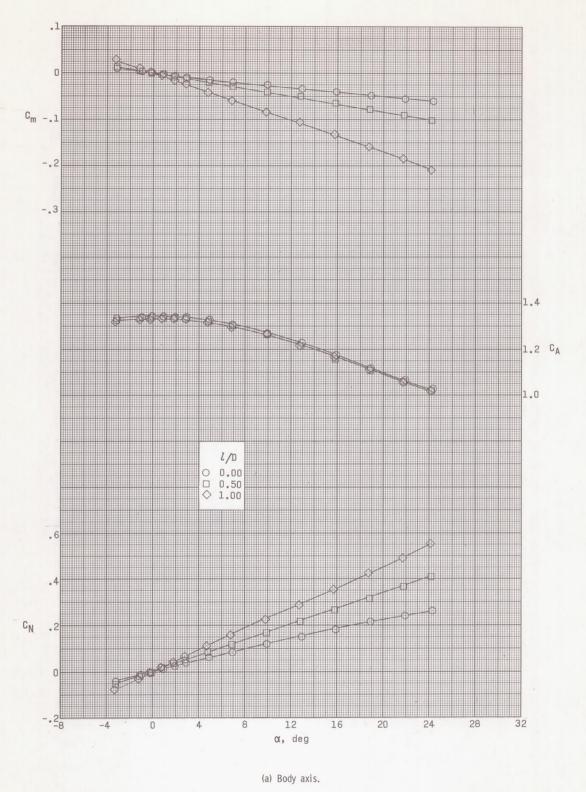
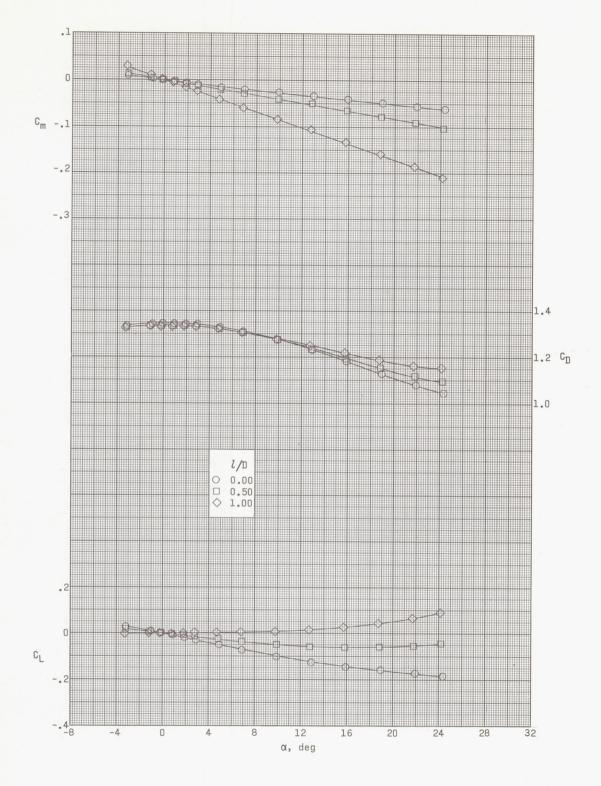


Figure 26.- Effect of cylinder length on longitudinal aerodynamic characteristics of  $50^{\circ}$  semiapex angle cone at M = 4.63.



(b) Stability axis.

Figure 26.- Concluded.

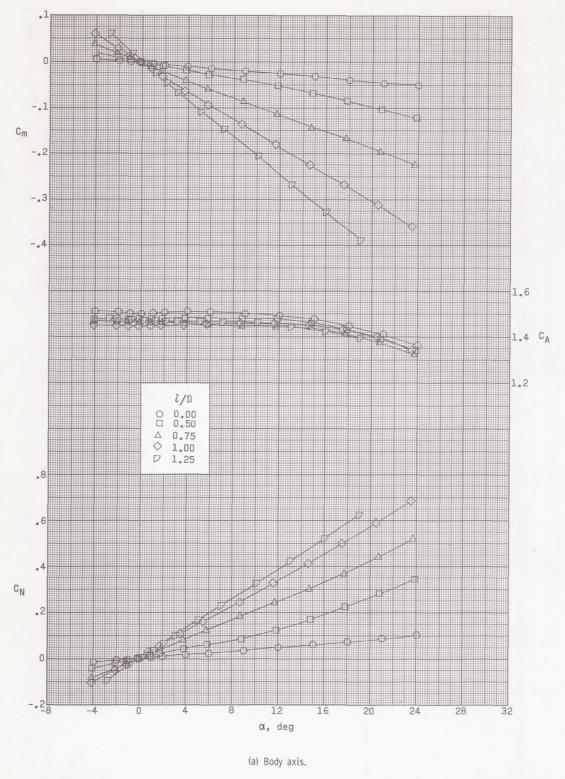
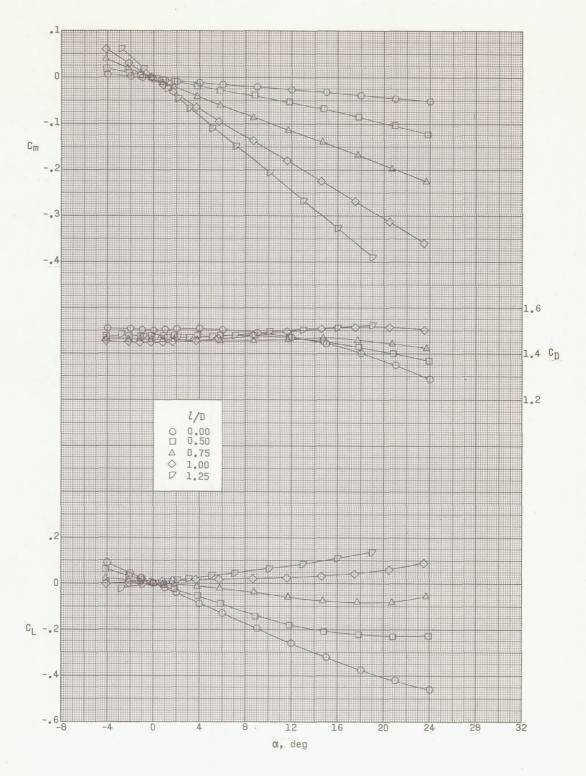


Figure 27.- Effect of cylinder length on longitudinal aerodynamic characteristics of  $60^{\circ}$  semiapex angle cone at M = 2.00.



(b) Stability axis.

Figure 27.- Concluded.

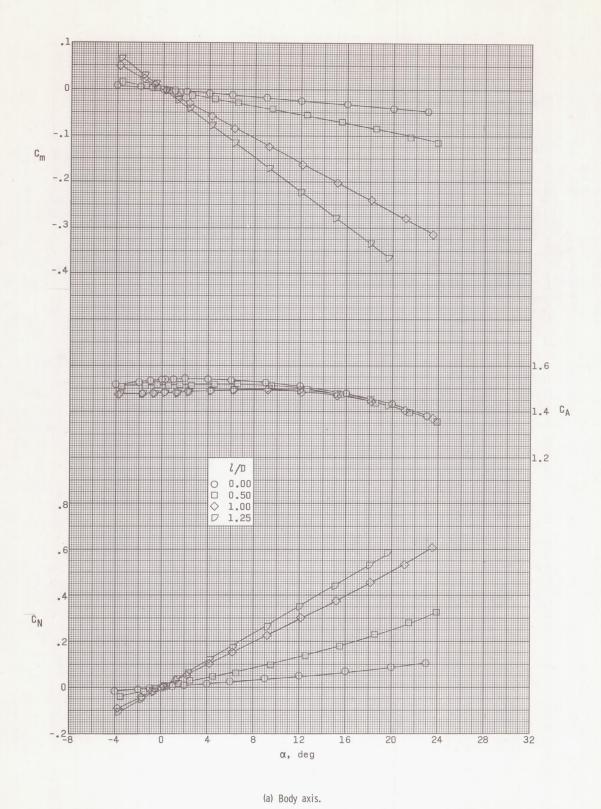
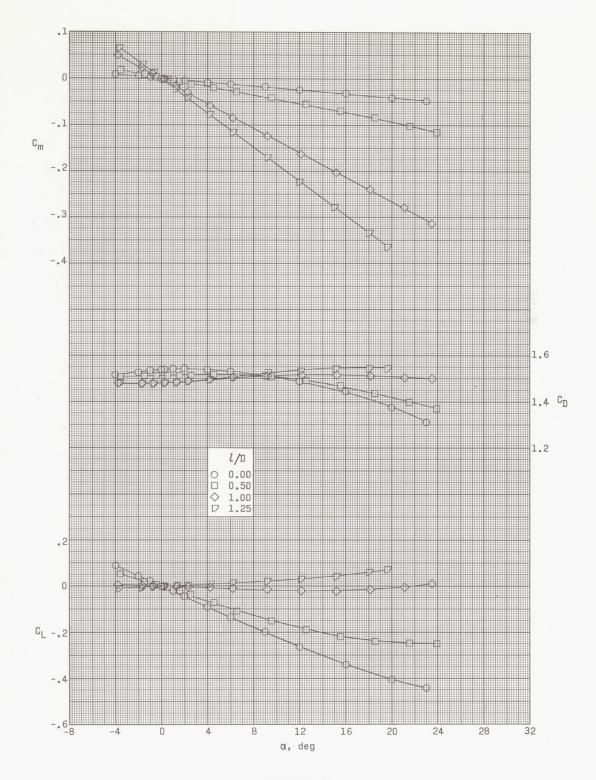


Figure 28.- Effect of cylinder length on longitudinal aerodynamic characteristics of  $60^{\circ}$  semiapex angle cone at M = 2.30. Data for  $\ell/D = 0$  from reference 6.



(b) Stability axis.

Figure 28.- Concluded.

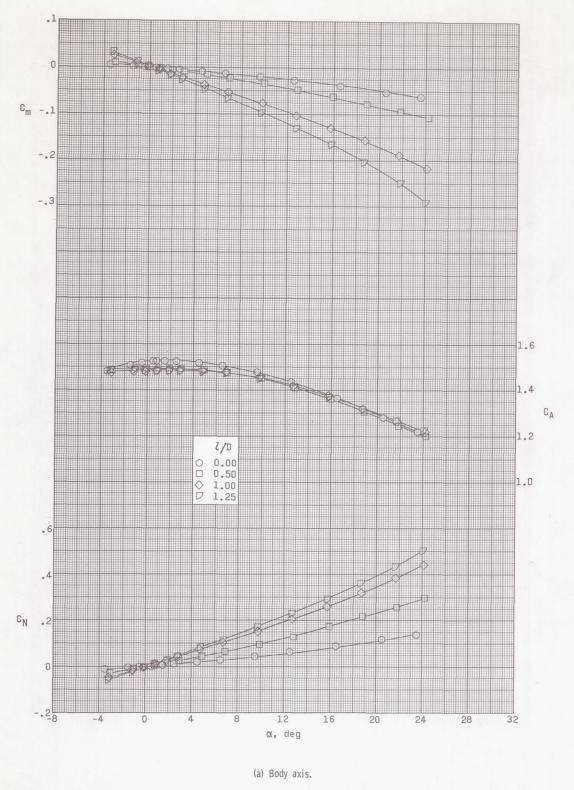
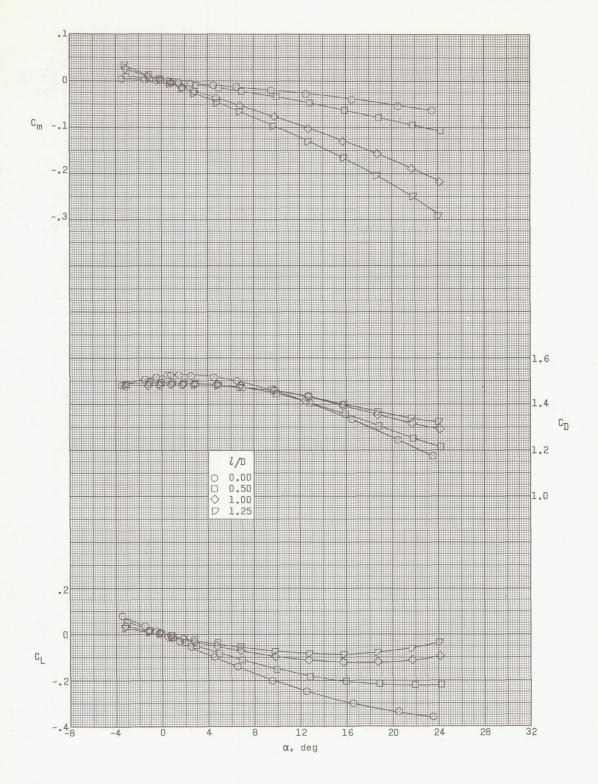


Figure 29.- Effect of cylinder length on longitudinal aerodynamic characteristics of  $60^{\circ}$  semiapex angle cone at M = 4.63. Data for l/D = 0 from reference 6.



(b) Stability axis.

Figure 29.- Concluded.

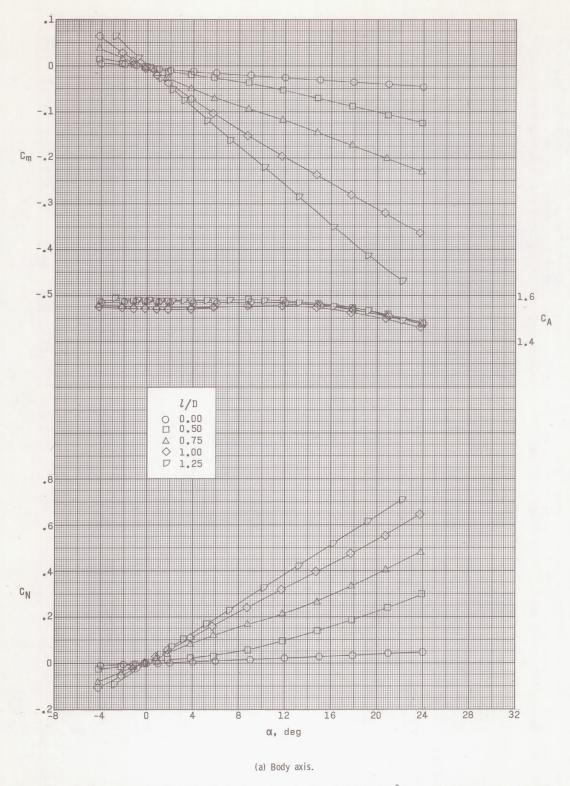
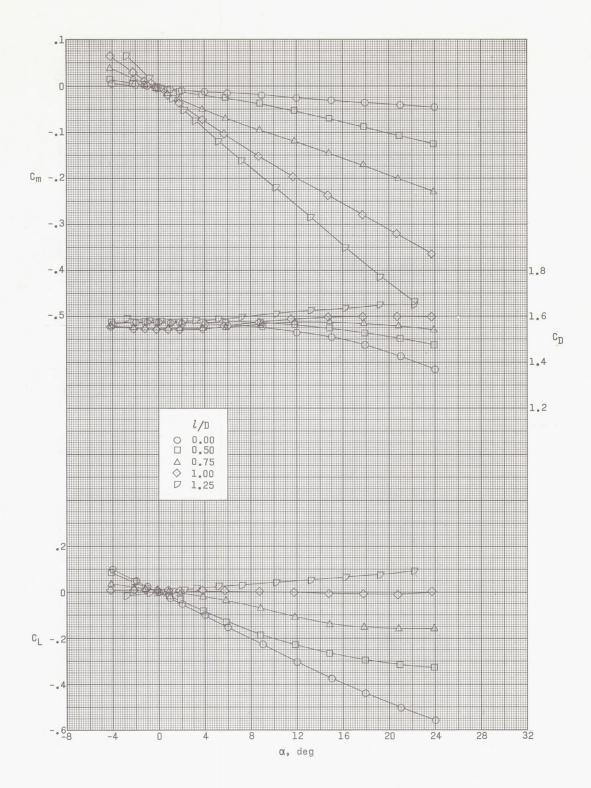


Figure 30.- Effect of cylinder length on longitudinal aerodynamic characteristics of  $70^{\circ}$  semiapex angle cone at M = 2.00.



(b) Stability axis.

Figure 30.- Concluded.

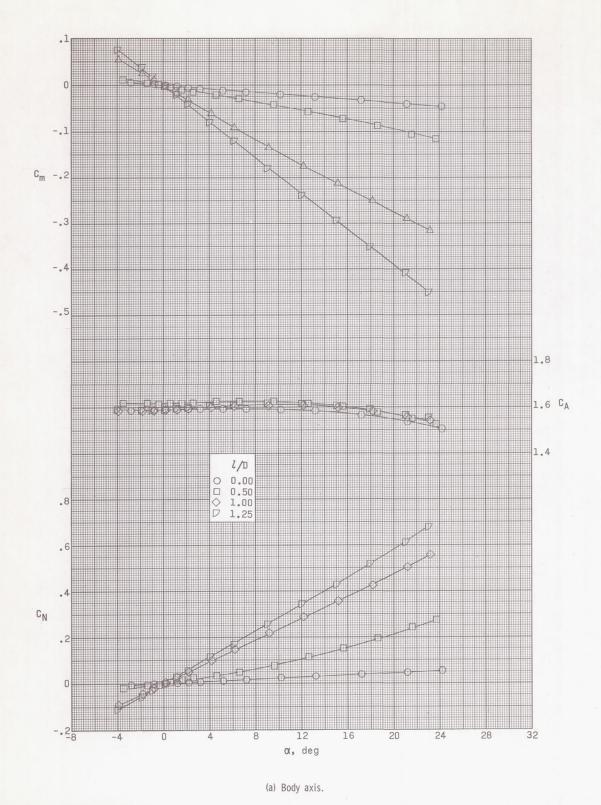
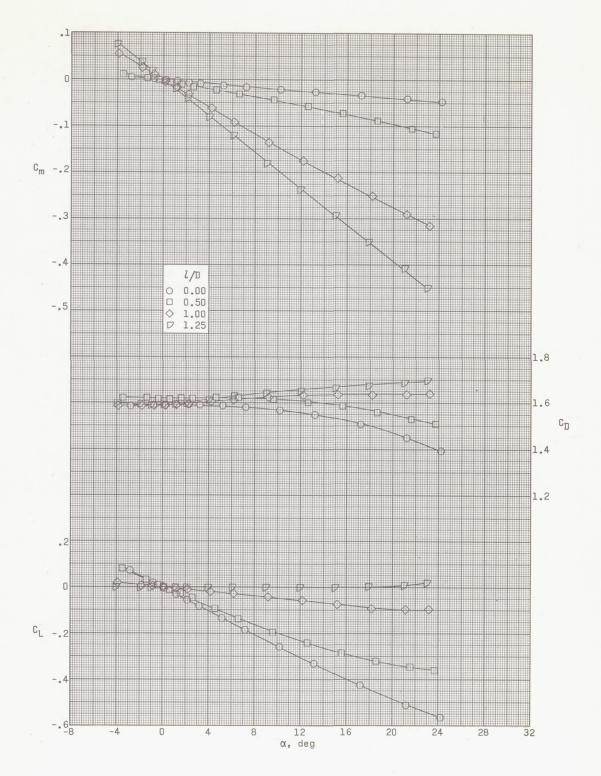


Figure 31.- Effect of cylinder length on longitudinal aerodynamic characteristics of  $70^{0}$  semiapex angle cone at M = 2.30. Data for  $\mathcal{I}/D = 0$  from reference 6.



(b) Stability axis.

Figure 31.- Concluded.

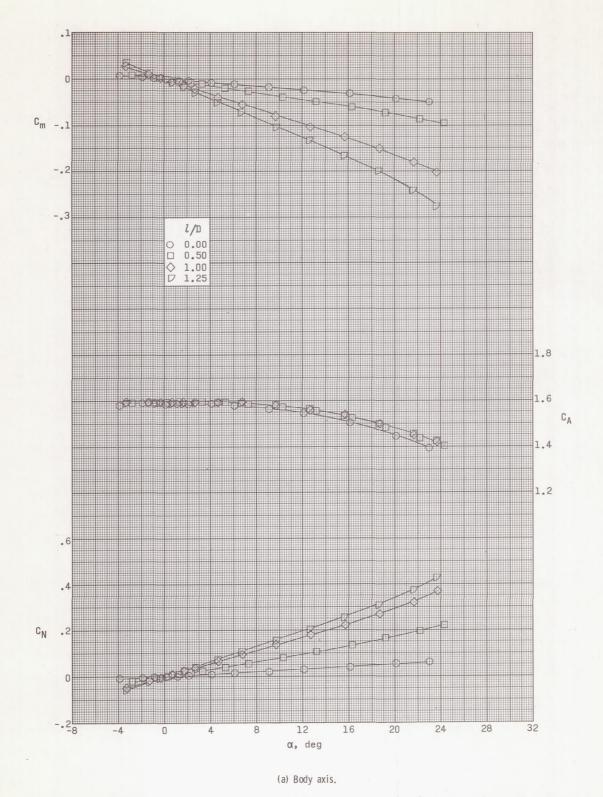
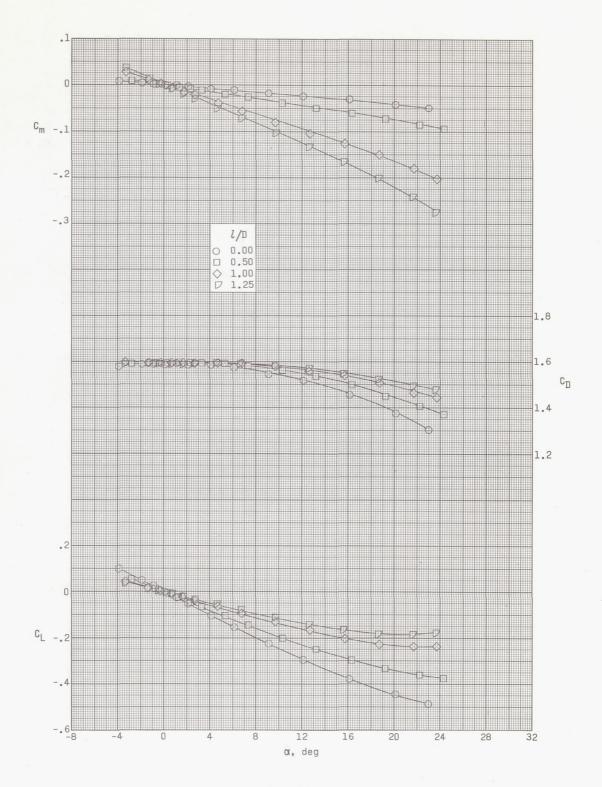


Figure 32.- Effect of cylinder length on longitudinal aerodynamic characteristics of  $70^{\circ}$  semiapex angle cone at M = 4.63. Data for 1/D = 0 from reference 6.



(b) Stability axis.

Figure 32.- Concluded.

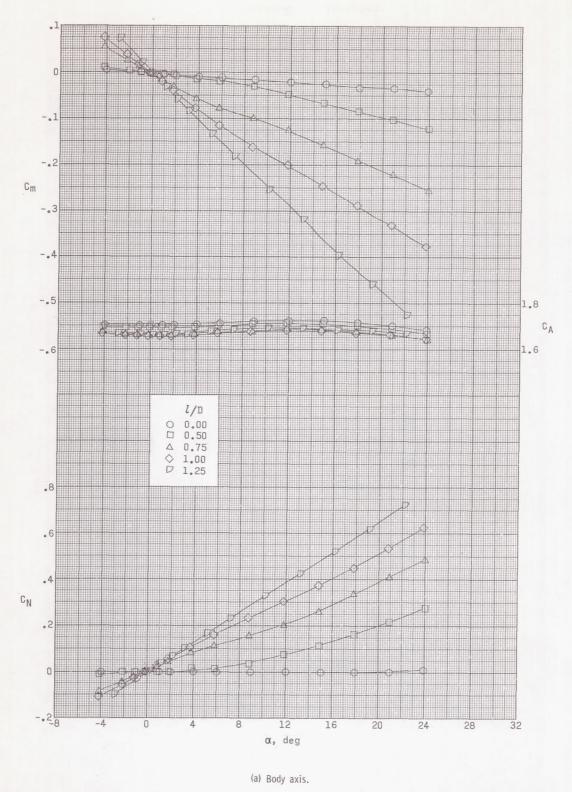
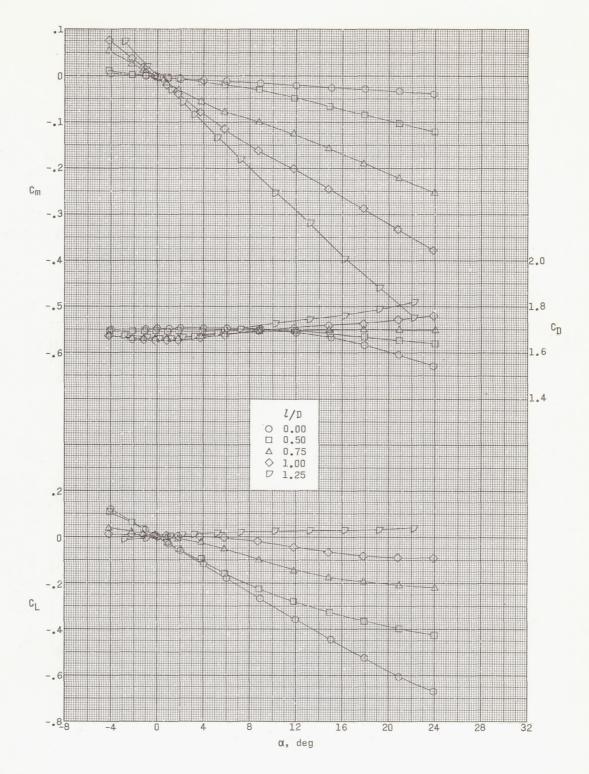


Figure 33.- Effect of cylinder length on longitudinal aerodynamic characteristics of  $90^{\circ}$  semiapex angle cone at M = 2.00.



(b) Stability axis.

Figure 33.- Concluded.

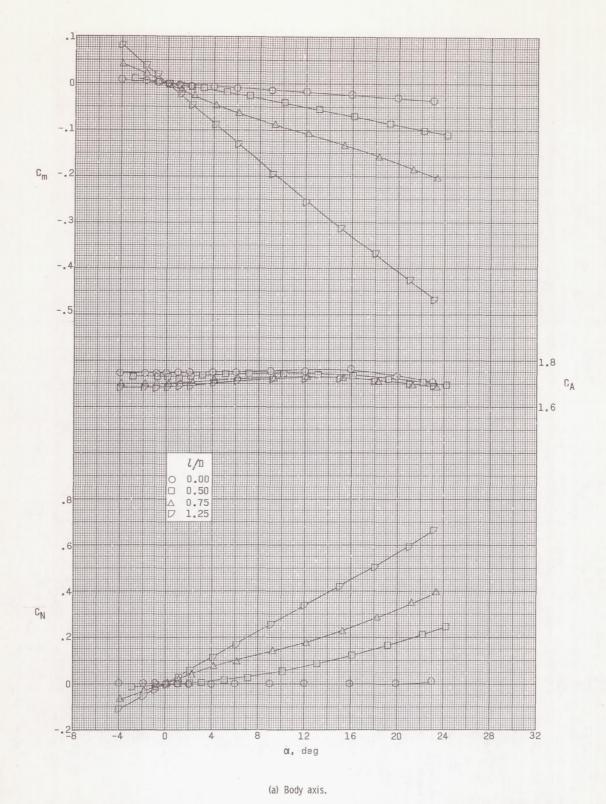
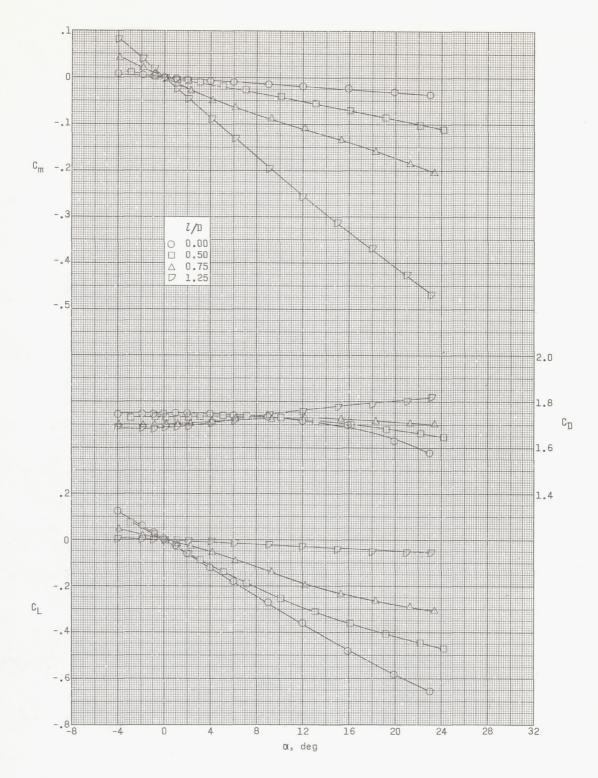


Figure 34.- Effect of cylinder length on longitudinal aerodynamic characteristics of  $90^{\circ}$  semiapex angle cone at M = 2.30. Data for 1/D = 0 from reference 6.



(b) Stability axis.

Figure 34.- Concluded.

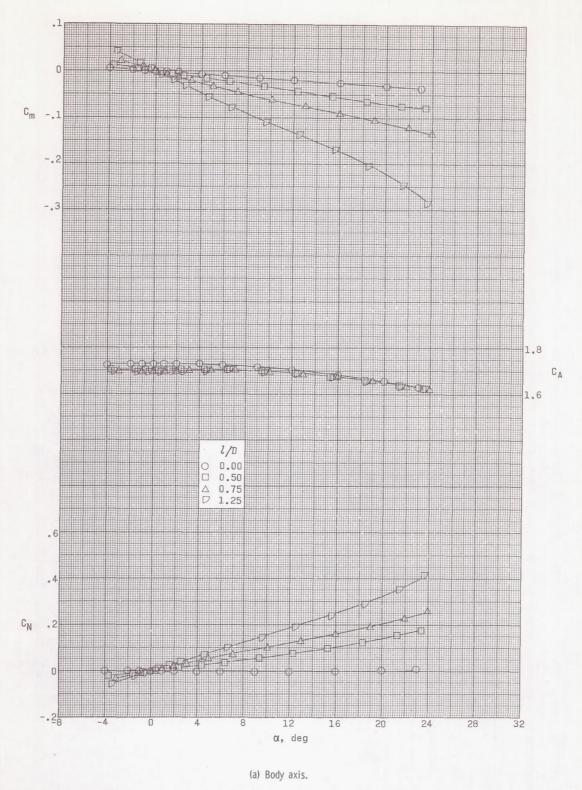
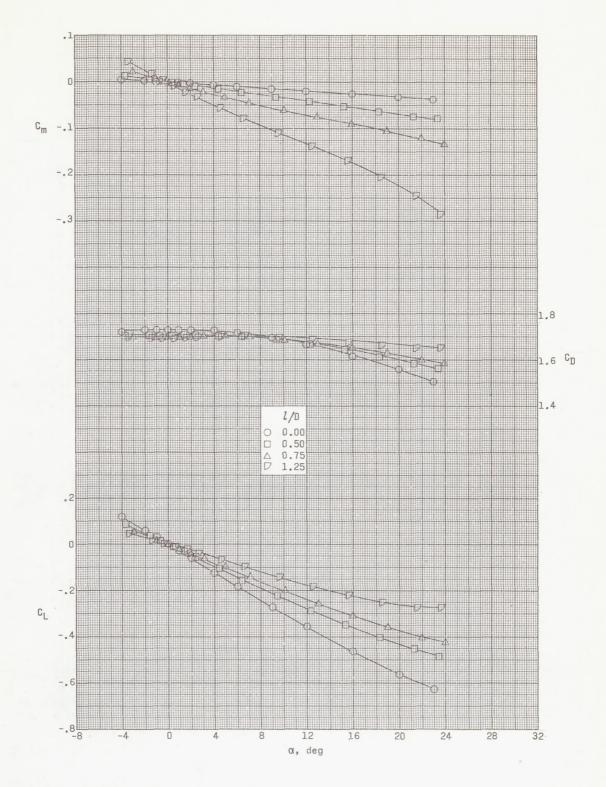


Figure 35.- Effect of cylinder length on longitudinal aerodynamic characteristics of  $90^{\circ}$  semiapex angle cone at M = 4.63. Data for l/D = 0 from reference 6.



(b) Stability axis.

Figure 35.- Concluded.

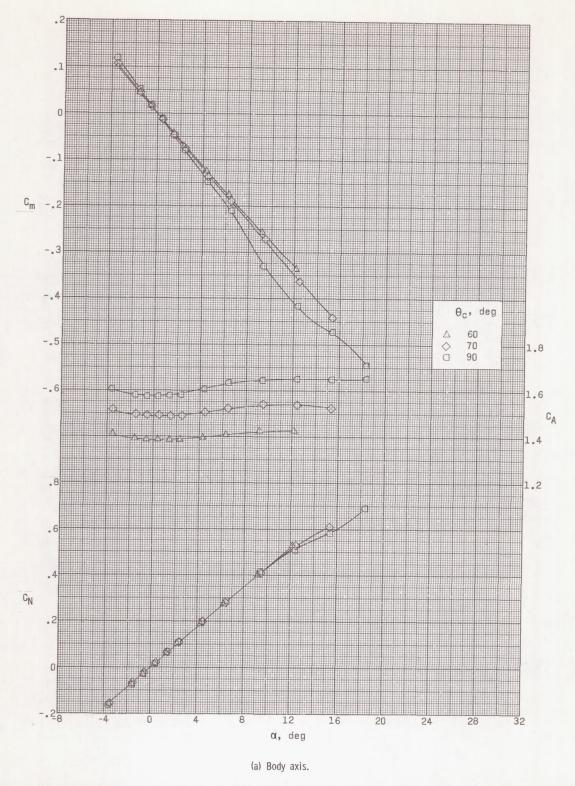
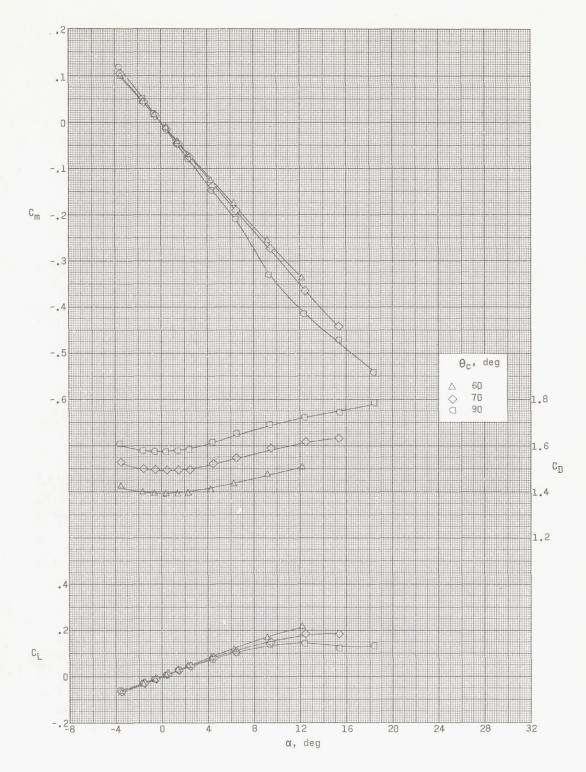


Figure 36.- Variation of longitudinal aerodynamic characteristics with angle of attack for cone-cylinder configurations with several semiapex angles and L/D = 1.25 for M = 1.50.



(b) Stability axis.

Figure 36.- Concluded.

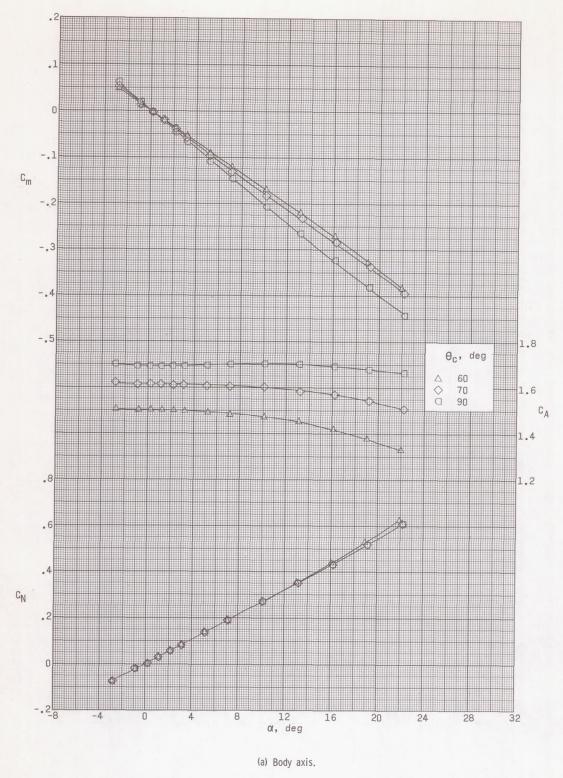
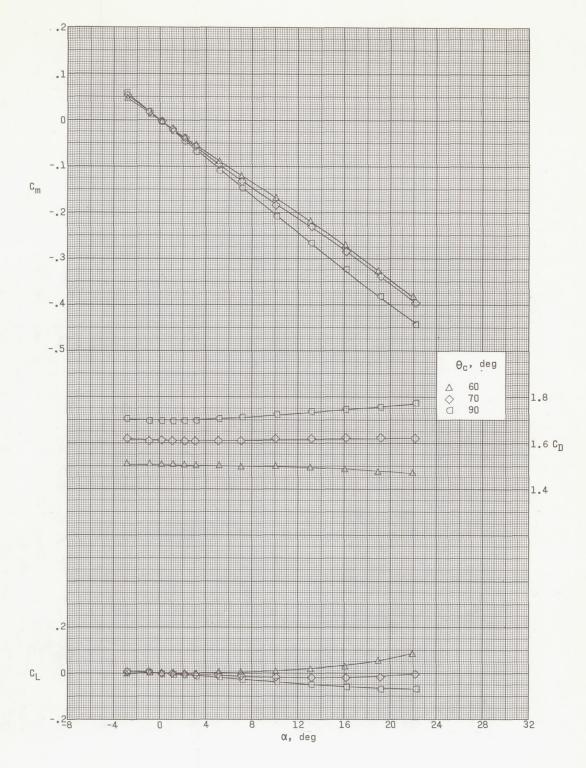


Figure 37.- Variation of longitudinal aerodynamic characteristics with angle of attack for cone-cylinder configurations with several semiapex angles and I/D = 1.25 for M = 2.50.



(b) Stability axis.

Figure 37.- Concluded.

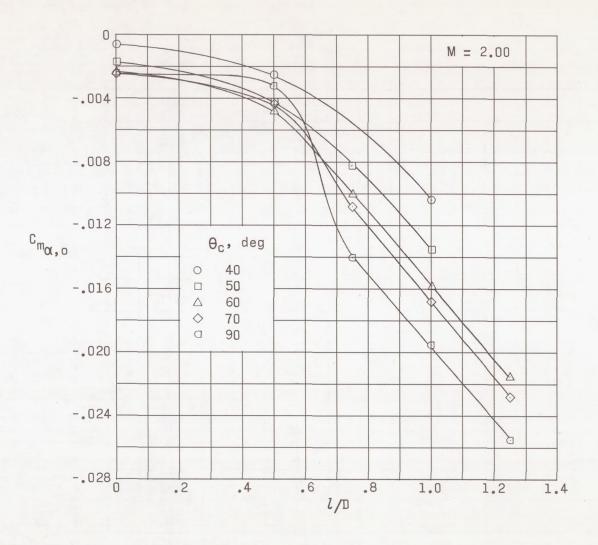


Figure 38.- Variation of pitching-moment-curve slope at zero angle of attack with nondimensionalized cylinder length for family of cone-cylinder models.

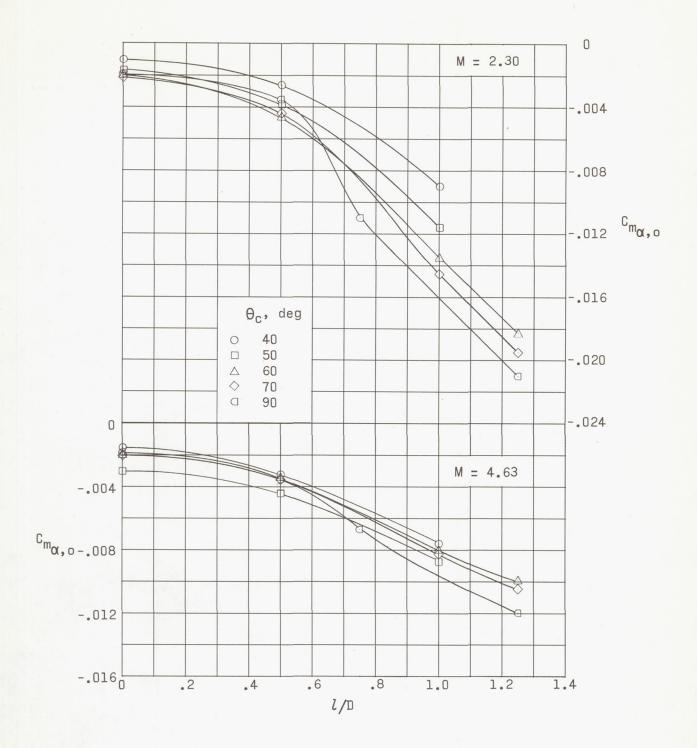


Figure 38.- Concluded.

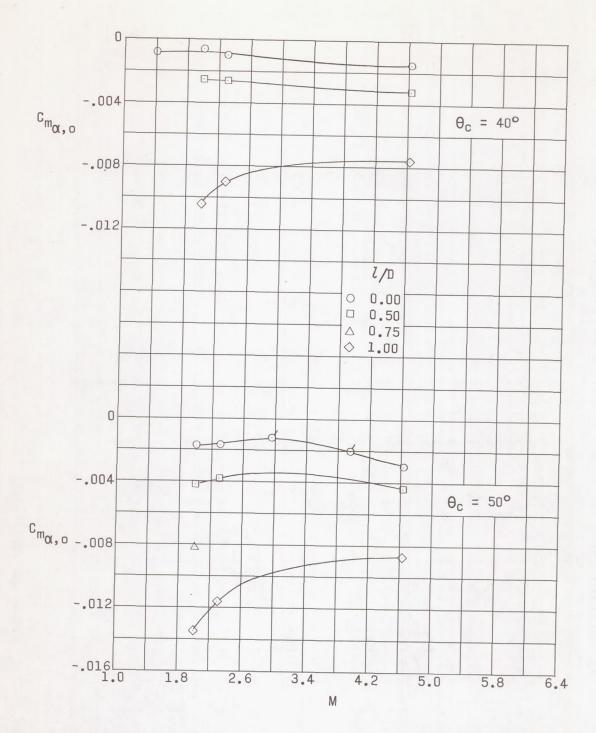


Figure 39.- Variation of pitching-moment-curve slope at zero angle of attack with Mach number for family of cone-cylinder models.

Ticked symbols from reference 6.

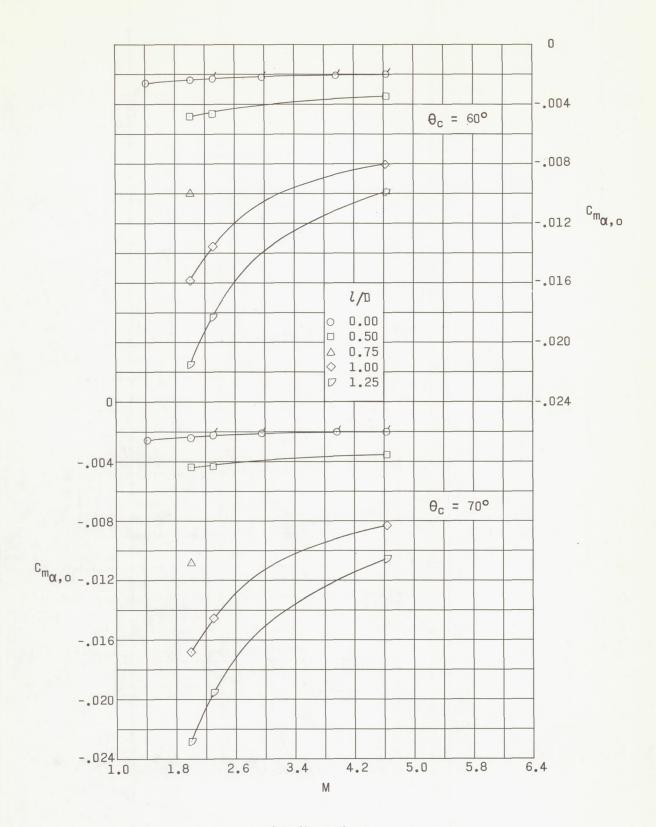


Figure 39.- Continued.

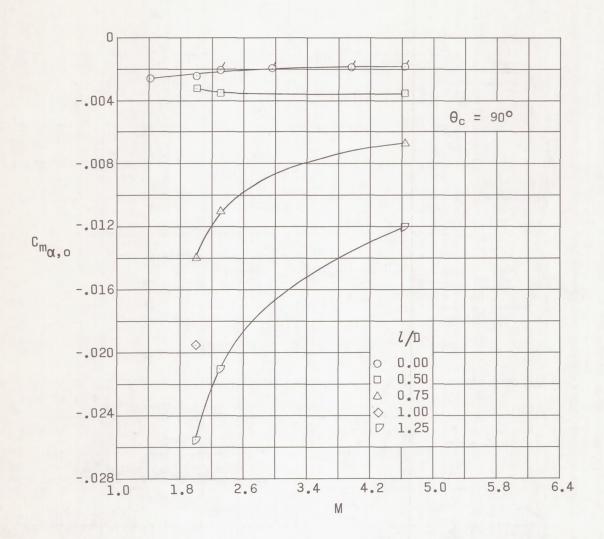


Figure 39.- Concluded.

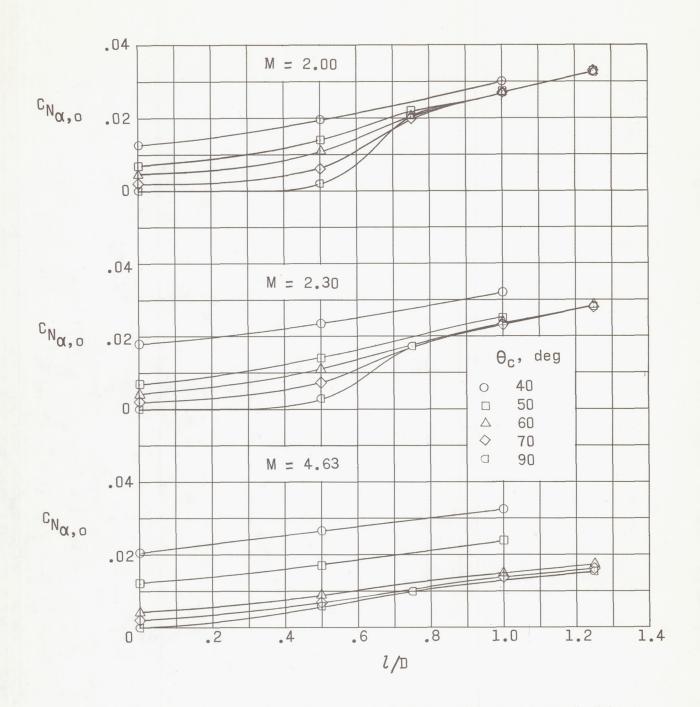


Figure 40.- Variation of normal-force-curve slope at zero angle of attack with nondimensionalized cylinder length for family of cone-cylinder models.

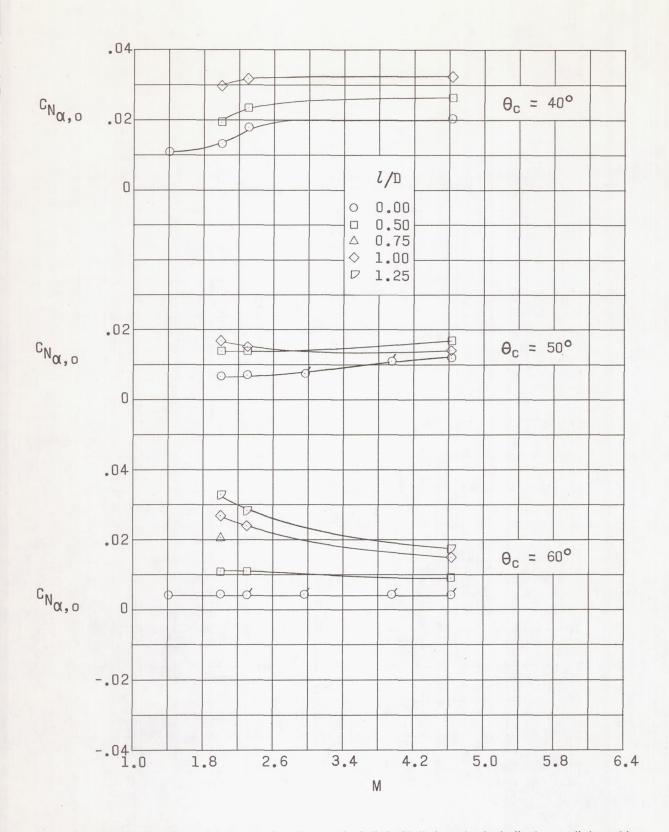


Figure 41.- Variation of normal-force-curve slope at zero angle of attack with Mach number for family of cone-cylinder models.

Ticked symbols from reference 6.

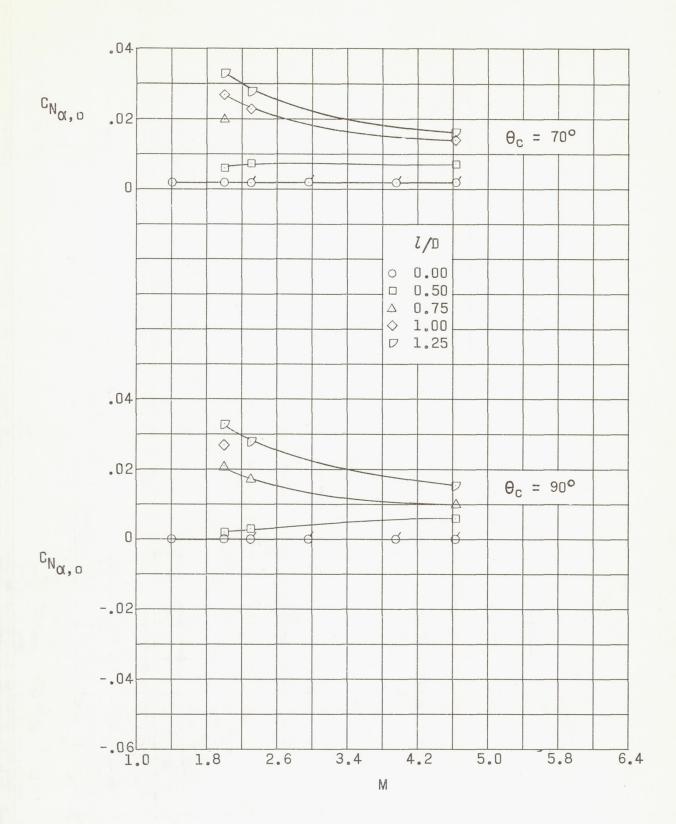


Figure 41.- Concluded.

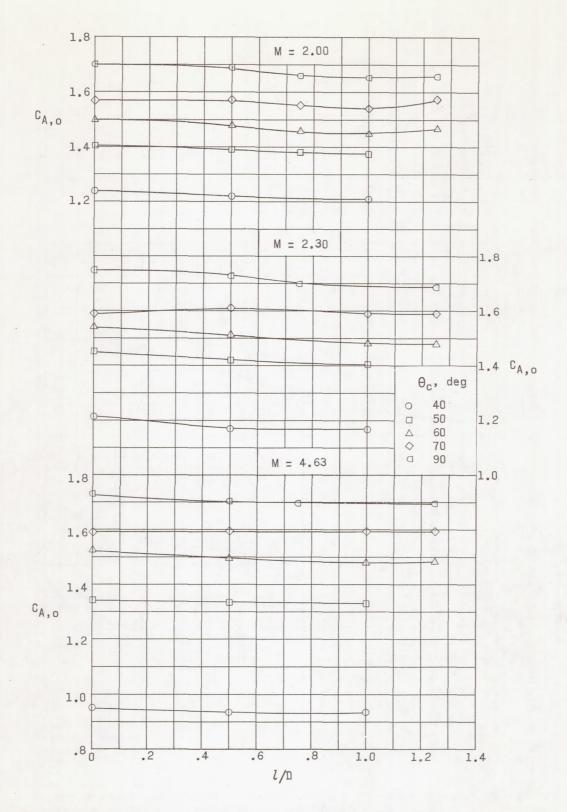


Figure 42.- Variation of axial-force coefficient at zero angle of attack with nondimensionalized cylinder length for family of cone-cylinder models.

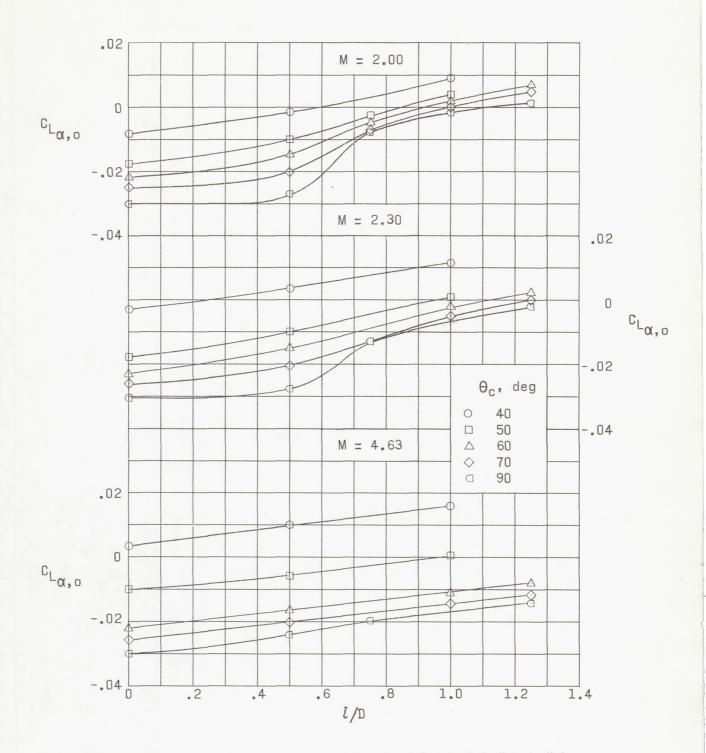


Figure 43.- Variation of lift-curve slope at zero angle of attack with nondimensionalized cylinder length for family of cone-cylinder models.

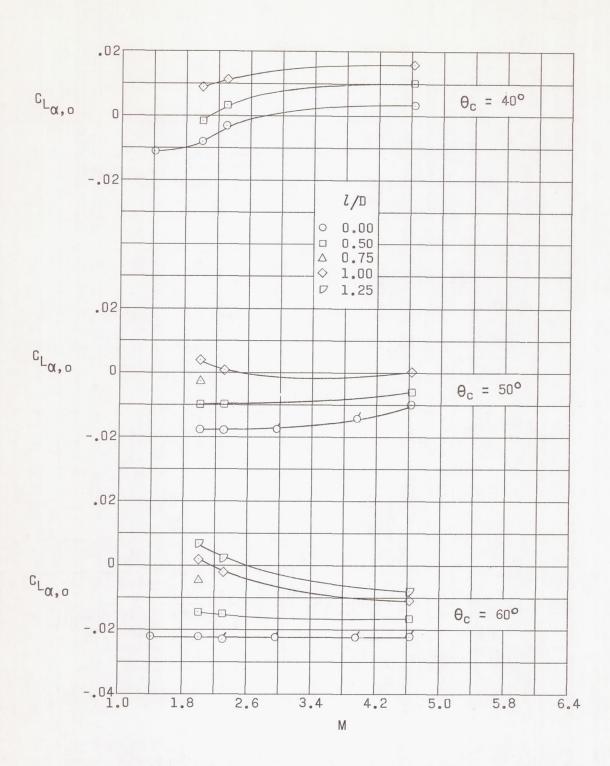


Figure 44.- Variation of lift-curve slope at zero angle of attack with Mach number for family of cone-cylinder models.

Ticked symbols from reference 6.

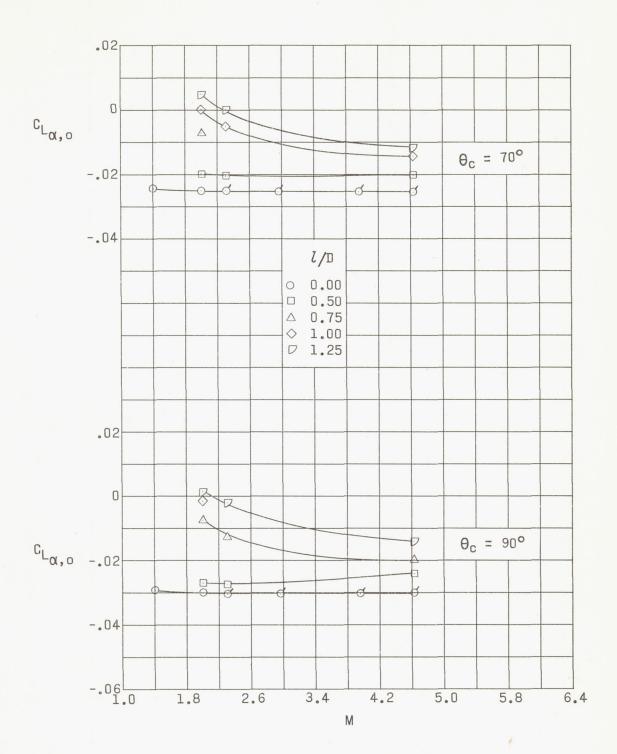


Figure 44.- Concluded.